Unified integral model for the lock-release and cooling-source gravity currents

Yangyue Zhang [*] and Ruifeng Hu [†]
Center for Particle-Laden Turbulence, Key Laboratory of Mechanics on Disaster and Environment in Western China, Ministry of Education, and College of Civil Engineering and Mechanics, Lanzhou University, Lanzhou 730000, People's Republic of China

(Received 28 December 2021; accepted 31 May 2022; published 13 June 2022)

A natural and sensible way of modeling the downburst outflow that triggers thunderstorms and sandstorms is regarding it as a gravity current sustained by the cooling source, which may be quite different from the lock-release gravity current. In this paper, a unified integral model incorporating a continuous velocity transition is proposed for the lock-release and cooling-source gravity currents. It suggests that the Froude number will increase by involving the shear layer in the dense fluid, the influence of which almost vanishes in the lock-release gravity current. The integral model for the cooling-source gravity current correlates the front characteristics with the thermodynamic and geometric properties of the cooling source, in good agreement with direct numerical simulations. Both the integral model and simulations indicate that the shear layer in the dense fluid could play a dominant role in the cooling-source gravity current. Results also demonstrate that the dimensionless front velocity and the front depth are governed by the center height and the longitudinal radius of the cooling source, barely affected by the vertical radius of the cooling source. The Froude number based on the center height of the cooling source is found to manifest a minor reliance on the geometric properties of the cooling source.

DOI: 10.1103/PhysRevFluids.7.063801

I. INTRODUCTION

The downburst outflow which gives rise to thunderstorms and convective sandstorms is essentially a gravity current [1–7]. The evaporation of precipitation in the cloud forms a mass of air that is cooler and heavier than the ambient. The descending fluid hits the earth's surface and spreads longitudinally in the ambient, generating a propagating front. The cooling source model [8–13] has been employed to represent the thermodynamic cooling effect of evaporating precipitation. Accordingly, the downburst outflow can be regarded as a gravity current generated by the cooling source, which will be referred to as the cooling-source gravity current. Studies on the cooling-source gravity current did not provide any appropriate methods to relate the outflow features with the properties of the cooling source. Oreskovic [14] introduced the scaling approach for a liquid drop release [15] and claimed that it appears to work well. Unfortunately, a limited number of cases and the absence of theoretical derivations make it unreliable. Moreover, the driving mechanisms of gravity currents produced by an elevated negatively buoyant thermal [16–18] and an elevated cooling source could be quite different. Therefore, no sophisticated theories and scaling methods have been established for the description of the cooling-source gravity current to the best of the authors' knowledge.

[*] zhangyy16@lzu.edu.cn
[†] hurf@lzu.edu.cn

 ©2022 American Physical Society

Various aspects of the gravity current have been studied [19], and a systematic overview is provided by Meiburg *et al.* [5]. A wide variety of strategies have been adopted, ranging from the integral models that determine the front velocity without resolving all of the interior features and the depth-averaged models [20–25] that provide an insight into different stages of the flow to the depth-resolving simulations [26–30] that explore detailed physics and turbulent structures. This paper focuses on the integral model, so a brief review of it will be given. The idealized model relating the front velocity with the front depth and the density difference between the heavier and lighter fluids was proposed by von Kármán [31], and Benjamin [32] improved it and developed a model based on mass conservation and momentum balance encompassing the front. Shin *et al.* [33] and Ungarish [34,35] resorted to global energy considerations to derive the Froude number of the lock-release gravity current. Several studies invoked the vorticity-based approach, which avoids energy-conserving arguments [36,37]. More recently, Ungarish and Hogg [38] presented a vortex-wake model unifying previous works by introducing a velocity transition layer [39] in the ambient. It is necessary to distinguish gravity currents created by releasing a finite volume of dense fluid and a cooling source, and most of these models concentrate on the lock-release flow. Little is known about the applicability of previous integral models on the cooling-source gravity current.

In this paper, a unified integral model for the lock-release and cooling-source gravity currents is proposed, and we check its feasibility by conducting direct numerical simulations. The paper is organized as follows. An integral model that incorporates a continuous velocity transition across the density interface at the front is developed in Sec. II. The integral model suitable for the lock-release gravity current is further established in Sec. III. The front features of the cooling-source gravity current are correlated with the thermodynamic and geometric properties of the cooling source in Sec. IV. We carry out direct numerical simulations of the cooling-source gravity current and discuss the applicability of the integral model in Sec. V. The conclusion of the paper is drawn in Sec. VI.

II. INTEGRAL MODEL CONCERNING THE FRONT

We confine the problem that the density difference between the heavier and lighter fluids is relatively small, justifying the adoption of the Boussinesq approximation [40]. Thus, the budget equations for the Boussinesq gravity current take the following dimensional form:

$$\frac{\partial u_j}{\partial x_j} = 0, \tag{1}$$

$$\frac{\partial u_i}{\partial t} + \frac{\partial u_i u_j}{\partial x_j} = -\frac{1}{\rho_0}\frac{\partial p}{\partial x_i} + \nu\frac{\partial^2 u_i}{\partial x_j x_j} + \frac{\rho g}{\rho_0} e_i{}^g, \tag{2}$$

$$\frac{\partial \rho}{\partial t} + \frac{\partial \rho u_j}{\partial x_j} = \alpha_\rho \frac{\partial^2 \rho}{\partial x_j x_j} + S_\rho, \tag{3}$$

where u_i is the flow velocity, x_i is the Cartesian coordinate, ρ is the density, p is the pressure, $e_i{}^g$ is the unit vector pointing in the direction of gravity, g is the gravitational acceleration, ν is the kinematic viscosity, and α_ρ denotes the molecular diffusion coefficient of the density field. ρ_0 is the reference density, set to the density in the ambient for convenience. S_ρ is the source term in the density budget equation.

The integral model will be established for the unsteady flow in the static reference frame as displayed in Fig. 1. We follow the assumption of the vortex-wake model [38] that the viscous and rotational effects exist close to the density interface, giving rise to a shear layer along the current-ambient interface. Taking a vertical integral of the viscous term $\nu\partial^2 u/\partial z^2$ spanning the entire depth yields zero, since the bottom and top boundaries are slip. Along the bottom and top walls, the viscous term $\nu\partial^2 u/\partial z^2$ is equal to $\nu\partial\omega/\partial z$, which vanishes owing to the assumption that the flow is mostly irrotational on and near the bottom and top boundaries. The independence of the velocity field on the longitudinal coordinate at cg and di is used to eliminate the viscous term $\nu\partial^2 u/\partial x^2$. Hence,

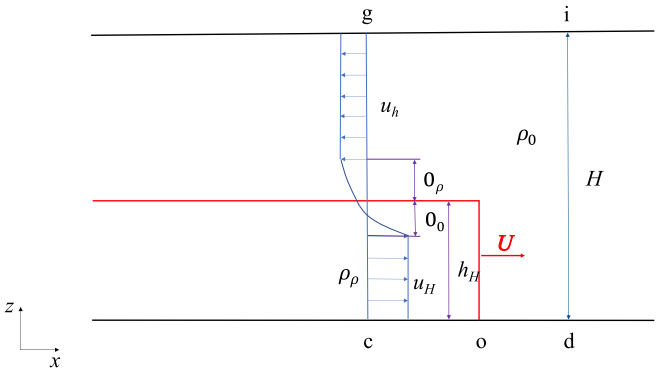

FIG. 1. A schematic of a two-dimensional gravity current. A gravity current advances in the ambient with a front velocity of U. The red solid line represents the density interface.

the momentum balance and pressure compatibility in the following derivation will not include the viscous effect explicitly. At the front of the gravity current, an upper velocity transition layer in the ambient and a lower velocity transition layer in the dense fluid are considered. The mixing of density is neglected, leading to a discontinuous density interface. The front is assumed to maintain a steady propagation along the longitudinal direction.

The longitudinal velocity profile at the front of cg is given by

$$u = \begin{cases} u_c, & 0 < z < h_c - \eta_l \\ u_c + (u_g - u_c)\phi_f\left(\frac{z-h_c+\eta_l}{\eta_l+\eta_u}\right), & h_c - \eta_l < z < h_c + \eta_u \\ u_g, & h_c + \eta_u < z < H, \end{cases} \tag{4}$$

where h_c is the front depth, η_l is the thickness of the lower velocity transition layer, and η_u is the thickness of the upper velocity transition layer. ϕ_f is a monotonically increasing function, which should satisfy $\phi_f(0) = 0$ and $\phi_f(1) = 1$. The density profile at cg is simply

$$\rho = \begin{cases} \rho_c, & 0 < z < h_c \\ \rho_0, & h_c < z < H. \end{cases} \tag{5}$$

First, consider the control volume of $cgdi$, consisting of two vertical planes and the top and bottom boundaries of the channel. Continuity implies that

$$\int_c^g u dz = 0. \tag{6}$$

Then, integrating the density budget equation in the control volume of $cgdi$ indicates that the increment of the density related to the propagating front is equal to the density flux at the front, i.e.,

$$U]\left(\int_c^g \rho dz - \int_d^i \rho dz\right) = \int_c^g \rho u dz. \tag{7}$$

We adopt the hydrostatic balance $\partial p/\partial z = -\rho g$ to obtain the pressure distribution at cg,

$$p = \begin{cases} p_c - \rho_c g z, & 0 < z < h_c \\ p_c - \rho_c g h_c - \rho_0 g(z - h_c), & h_c < z < H, \end{cases} \tag{8}$$

and at di:

$$p = p_d - \rho_0 g z. \tag{9}$$

The pressure differences between the bottom and top boundaries are evaluated by

$$p_c - p_g = \rho_0 g(H - h_c) + \rho_c g h_c, \tag{10}$$

$$p_d - p_i = \rho_0 g H. \tag{11}$$

The unsteady Bernoulli equations are applied along cd and gi, respectively, yielding

$$p_i - p_g = \tfrac{1}{2}\rho_0 u_g^2 - \rho_0 U u_g, \tag{12}$$

$$p_d - p_c = \tfrac{1}{2}\rho_c u_c^2 - \rho_c U u_c. \tag{13}$$

These pressure differences should satisfy consistency to guarantee that the pressure field is single valued, resulting in

$$-(\rho_c - \rho_0) g h_c + \tfrac{1}{2}\rho_0 u_g^2 - \tfrac{1}{2}\rho_c u_c^2 + \rho_c U u_c - \rho_0 U u_g = 0. \tag{14}$$

Finally, integrating the longitudinal momentum budget equation in the control volume of $cgdi$ yields

$$U \int_c^g \rho u dz - \int_c^g (p + \rho u^2) dz + \int_d^i p dz = 0. \tag{15}$$

Substituting Eqs. (4), (5), (8), (9), and (13) into Eq. (15) leads to the final expression that is very complicated.

By neglecting the shear layer in the dense fluid and applying the Boussinesq approximation, the above derivation will be equivalent to the vortex-wake model [38]. The front velocity as a function of the front depth is not determinate, since an extra variable that is the thickness of the lower velocity transition layer is involved.

We impose two specific types of ϕ_f, linear and exponential profiles [38], i.e.,

$$\phi_f^l = z, \tag{16}$$

$$\phi_f^e = \frac{1 - e^{-\alpha z}}{1 - e^{-\alpha}}, \quad \alpha > 0. \tag{17}$$

α is set to 3 in the vortex-wake model [38] and we use multiple values 1, 3, and 5 to examine the effects. An exponential profile represents a sharper velocity transition from the bottom layer to the top layer compared with a linear profile.

The energy dissipation of the front in present static reference frame can be defined by the difference between the energy flux entering the control volume of $cgdi$ and the energy increment related to a steady propagation, i.e.,

$$\dot{\mathcal{D}} = \int_c^g \left(\frac{1}{2}\rho u^2 + p + \rho g z\right) u dz - U\left[\int_c^g \left(\frac{1}{2}\rho u^2 + \rho g z\right) dz - \int_d^i \rho g z dz\right], \tag{18}$$

which is equal to the energy dissipation calculated in the moving reference frame by combining the longitudinal momentum balance encompassing the front.

The Newton iterative method is implemented to solve Eqs. (6), (7), (14), and (15) numerically owing to the extreme difficulty of seeking an analytical solution. The Boussinesq approximation and the scaling method for the gravity current [5] are adopted as well.

The Froude number and the dimensionless energy dissipation as functions of the front depth for various thicknesses of the lower velocity transition layer are presented in Fig. 2. A decrease in the Froude number with the growing front depth is distinct. Compared with the vortex-wake model [38], introducing a lower velocity transition layer contributes to a growth of the Froude number. The effect of the lower velocity transition layer with a certain thickness is significant and then diminishes remarkably as the front depth increases. Another direct insight into the influence of the shear layer in

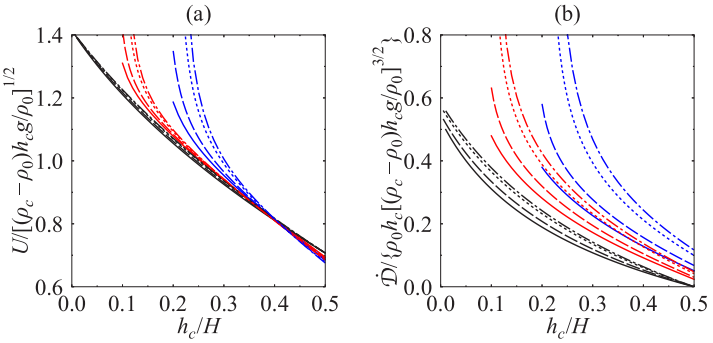

FIG. 2. The Froude number (a) and the dimensionless energy dissipation (b) as functions of the front depth for various thicknesses of the lower velocity transition layer: $\eta_l/H = 0$ (the vortex-wake model [38], black), 0.1 (red), 0.2 (blue). The velocity profile in the transition layer is assumed to be linear (solid line) and exponential with $\alpha = 1$ (dashed line), 3 (dotted line), 5 (dash-dotted line).

the dense fluid is shown in Fig. 3, which displays the Froude number and the dimensionless energy dissipation as functions of the relative thickness of the lower velocity transition layer for various front depths. In general, the Froude number exhibits a rising tendency with the enhanced shear layer in the dense fluid. As the lower velocity transition layer nearly occupies the depth of the dense fluid layer, the Froude number rises drastically for an exponential velocity transition with $\alpha = 3, 5$. The increase in the Froude number is accompanied by higher energy dissipation. The vortex-wake model predicts that the energy dissipation drops to zero as the front depth approaches $1/2$, and involving a lower velocity transition layer results in positive energy dissipation. An exponential velocity transition produces a larger Froude number and induces more energy dissipation than a linear velocity transition.

To unify the results with different functions of the velocity transition, we define a mixing coefficient to assess the effect of the shear layer in the dense fluid, i.e.,

$$\Phi_l = \frac{\int_0^{h_c} \frac{u-u_c}{u_g-u_c} dz}{h_c}. \tag{19}$$

As shown in Fig. 4(a), the mixing coefficient monotonically grows as the relative thickness of the lower velocity transition layer increases, influenced by the form of the velocity profile in the

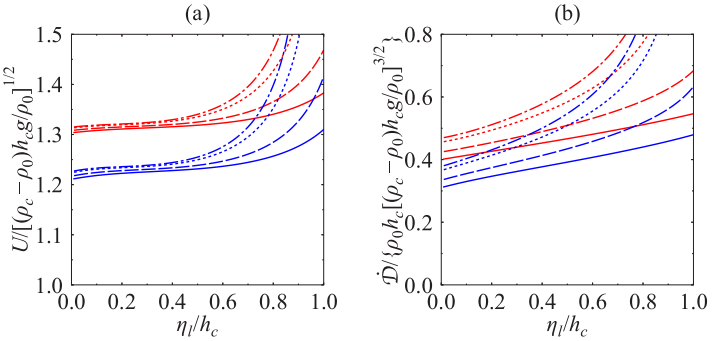

FIG. 3. The Froude number (a) and the dimensionless energy dissipation (b) as functions of the relative thickness of the lower velocity transition layer for various front depths: $h_c/H = 0.1$ (red), 0.2 (blue). The velocity profile in the transition layer is assumed to be linear (solid line) and exponential with $\alpha = 1$ (dashed line), 3 (dotted line), 5 (dash-dotted line).

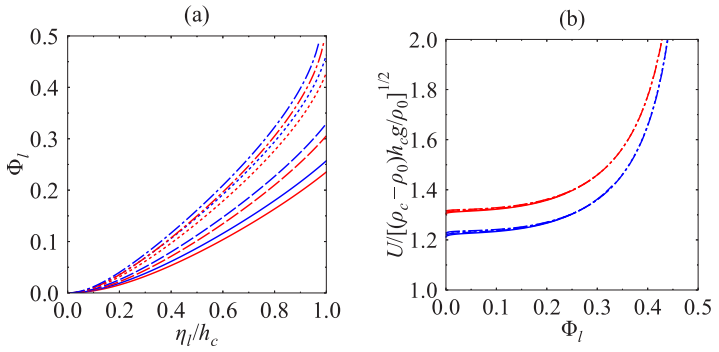

FIG. 4. (a) The mixing coefficient as a function of the relative thickness of the lower velocity transition layer. (b) The Froude number as a function of the mixing coefficient. Various front depths are included: h_c/H=0.1 (red), 0.2 (blue). The velocity profile in the transition layer is assumed to be linear (solid line) and exponential with $\alpha = 1$ (dashed line), 3 (dotted line), 5 (dash-dotted line).

transition layer. As presented in Fig. 4(b), the Froude number as a function of the mixing coefficient perfectly collapses for all velocity transitions, which demonstrates that the mixing coefficient provides a very good estimate of the effect of the shear layer in the dense fluid on the Froude number.

The formulation only contains the common characteristics of a steady advancing front so far and is irrelevant to the mechanism that the gravity current generates. To close the system of equations, we should take into consideration the conditions in the source region for the lock-release and cooling-source gravity currents, respectively.

III. CLOSURE FOR THE LOCK-RELEASE GRAVITY CURRENT

The configuration of the gravity current produced by a partial-depth lock release is displayed in Fig. 5. In the source region, a left-moving discontinuity propagates back into the lock.

First, the density is conserved in the control volume of *aedi,* since there is no density source, i.e.,

$$U_r\left(\int_b^f \rho dz - \int_{b'}^{f'} \rho dz\right) = U\left(\int_c^g \rho dz - \int_d^i \rho dz\right), \tag{20}$$

where U_r is the velocity of the left-moving discontinuity at *bf*.

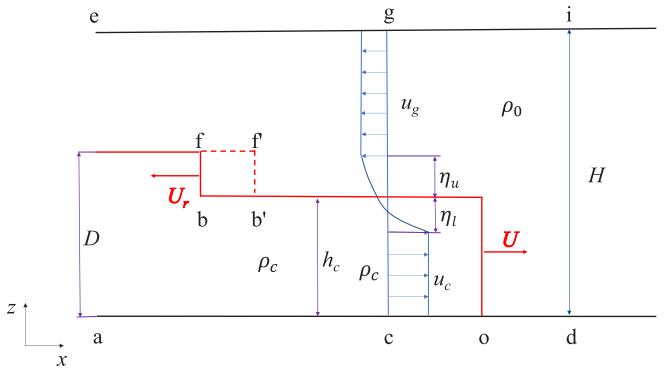

FIG. 5. A schematic of a partial-depth lock release. A gravity current advances in the ambient with a front velocity of U, and a left-moving discontinuity propagates back into the lock with a velocity of U_r.

The hydrostatic balance is justified at *ae*, and the density in the interior of the gravity current is assumed to not vary with the longitudinal position, resulting in a pressure distribution

$$p = \begin{cases} p_a - \rho_c g z, & 0 < z < D \\ p_a - \rho_c g D - \rho_0 g (z - D), & D < z < H, \end{cases} \tag{21}$$

where D denotes the lock depth. Thus, the pressure difference of *ae* is simply

$$p_a - p_e = \rho_0 g (H - D) + \rho_c g D. \tag{22}$$

The pressure differences along the top and bottom boundaries can be evaluated by applying the unsteady Bernoulli equations, which leads to

$$p_i - p_e = -\rho_0 (U + U_r) u_g, \tag{23}$$

$$p_d - p_a = -\rho_c (U + U_r) u_c. \tag{24}$$

A single-valued pressure field requires

$$-(\rho_c - \rho_0) g D - \rho_0 (U + U_r) u_g + \rho_c (U + U_r) u_c = 0. \tag{25}$$

Finally, integrating the longitudinal momentum budget equation in the control volume of *aedi* yields

$$(U + U_r) \int_c^g \rho u dz - \int_a^e p dz + \int_d^i p dz = 0. \tag{26}$$

The closure for the lock-release gravity current has been done, which relates the front features with the lock depth [33,36]. Equations (6), (7), (14), (15), (20), (25), and (26) will be simplified by the Boussinesq approximation and numerically solved with the Newton iterative method.

By utilizing the relationship between the lock depth and the front depth to eliminate the lock depth, we are able to obtain the Froude number, the dimensionless energy dissipation of the front, the relative thickness of the lower velocity transition layer, and the mixing coefficient as functions of the front depth as shown in Fig. 6. Previous integral models and direct numerical simulations of lock-release gravity currents are included for comparison. In addition, the thickness of the lower velocity transition layer as a function of the front depth measured by direct numerical simulations of Borden and Meiburg [36] is fitted and incorporated in the integral model that only considers the front and does not include the closure for the lock-release gravity current, denoted by present model V. Concerning the Froude number as a function of the front depth, our model is in good agreement with direct numerical simulations of Borden and Meiburg [36]. Our model predicts a relationship between the Froude number and the front depth, which is very close to previous integral models and nearly coincides with the vortex-wake model [38], implying that the effect of the shear layer in the dense fluid vanishes in the lock-release gravity current. The relative thickness of the lower velocity transition layer is slightly negative, that is, unphysical for an exponential velocity transition with $\alpha = 3, 5$, and it is positive and small for a linear velocity transition and an exponential velocity transition with $\alpha = 1$. Assuming different forms of the velocity profile barely influences the Froude number, but it possibly produces unphysical thicknesses of the lower velocity transition layer. Moreover, obvious differences in the relative thickness of the lower velocity transition layer are found between our model and direct numerical simulations of Borden and Meiburg [36], and the inconsistency of the definition may be responsible for this. Additionally, a left-moving discontinuity is not assured. The left front propagates as a rarefaction wave instead of a discontinuity when $D < H/2$ [19]. The experimental data of Rottman and Simpson [23] suggests an even stricter condition, i.e., a left-moving discontinuity will only appear when D/H is greater than about 0.7. Hence, this mismatch (expansion wave versus discontinuity) is likely to account for the thickness of the lower velocity transition layer becoming negative and deviating from the direct numerical

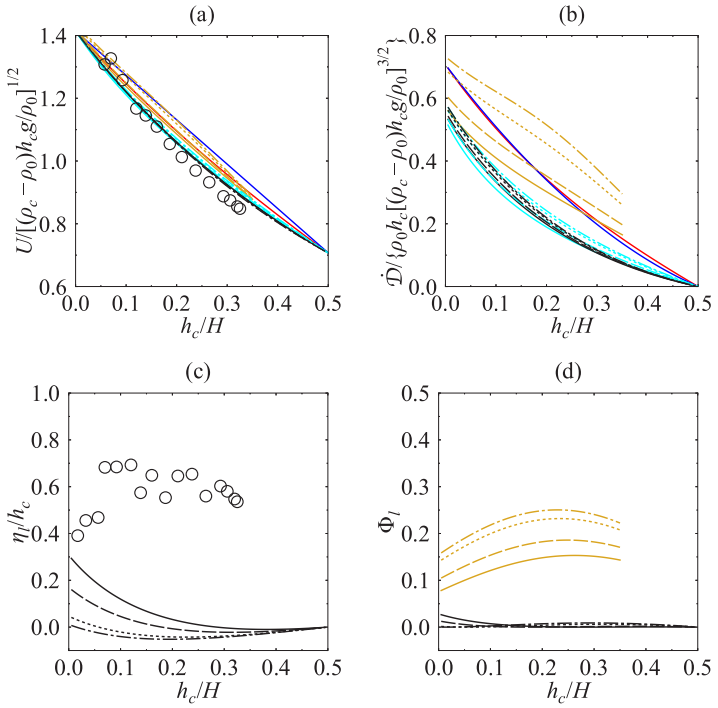

FIG. 6. The Froude number (a), the dimensionless energy dissipation of the front (b), and the relative thickness of the lower velocity transition layer (c), and the mixing coefficient (d) as functions of the front depth for various integral models: Benjamin [32] (red solid line), Borden and Meiburg [36] (blue solid line), Ungarish and Hogg [38] (cyan line), present model (black line), present model V (goldenrod line). The velocity profile in the transition layer is assumed to be linear (solid line) and exponential with $\alpha = 1$ (dashed line), 3 (dotted line), 5 (dash-dotted line). The symbols are results from direct numerical simulations of Borden and Meiburg [36].

simulations. Present model V that does not utilize the left-moving discontinuity offers a reasonable estimate of the Froude number, but obviously higher mixing coefficients are predicted. Nevertheless, the maximum mixing coefficient predicted by present model V is still below the criterion that the shear layer in the dense fluid has a distinct impact on the Froude number as shown in Fig. 4(b). The energy dissipation of the front from our model and the vortex-wake model is visibly lower, compared with integral models [32,36] that do not include a continuous velocity transition. As the front depth approaches $1/2$, the thickness of the lower velocity transition layer and the energy dissipation of the front all tend to be zero.

The vortex-wake model and Benjamin's model concerning the front of a general gravity current could not determine the front depth. Hence, the model that considers mass, momentum, and energy of the whole system [33] and the approach based on mass and vorticity of the entire domain [36], both of which relate the front depth with the lock depth, are presented. The relative front depth and the Froude number based on the lock depth as functions of the lock depth are displayed in Fig. 7. The vorticity-based model and our model both predict relative front depths smaller than $1/2$, which is directly given by the integral model containing energy arguments. The Froude number based on the lock depth from our model lies between that from the energy-based and vorticity-based approaches. The relative front depths all reach $1/2$ as the lock depth approaches 1, implying a full-depth release. Our model seems to provide a slightly improved prediction of the Froude number based on the lock depth. The Froude number based on the lock depth and the relative front depth are both merely affected by the function of the velocity transition.

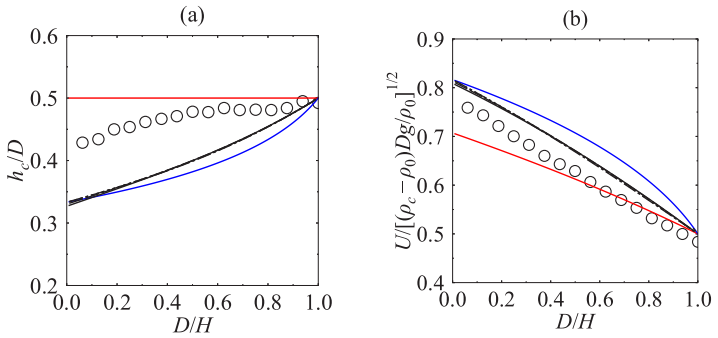

FIG. 7. The relative front depth (a) and the Froude number based on the lock depth (b) as functions of the lock depth for various integral models: Shin *et al.* [33] (red solid line), Borden and Meiburg [36] (blue solid line), present model (black line). The velocity profile in the transition layer is assumed to be linear (solid line) and exponential with $\alpha = 1$ (dashed line), 3 (dotted line), 5 (dash-dotted line). The symbols are results from direct numerical simulations of Borden and Meiburg [36].

IV. CLOSURE FOR THE COOLING-SOURCE GRAVITY CURRENT

The cooling source model specifies the temporary and spatial cooling rate during the evolution of a downburst event. Following the definition given by Anderson *et al.* [8] and Orf *et al.* [9], the cooling source function can be written as

$$q = \begin{cases} Q(t)\cos^2\frac{\pi R}{2}, & R < 1 \\ 0, & R > 1, \end{cases} \tag{27}$$

which is ellipsoidal in shape and uses a $\cos^2$ spatial ramp-up. R is the normalized position

$$R = \sqrt{\left(\frac{x}{r_x}\right)^2 + \left(\frac{z - z_0}{r_z}\right)^2}, \tag{28}$$

where r_x is the longitudinal radius of the cooling source, r_z is the vertical radius of the cooling source, and z_0 is the center height of the cooling source. $Q(t)$ is the temporary cooling rate, which contains an initial $\cos^2$ ramp-up stage, followed by a steady state, and then a $\cos^2$ decaying period. We consider a constant temporary cooling rate in this study to maintain a constant Reynolds number and to exclude the influence of its variation, i.e.,

$$Q(t) = Q_m. \tag{29}$$

The simplification may not be appropriate for a real natural event but makes it easier for us to concentrate on the essence of the cooling-source gravity current.

The areal integral of the cooling source function can measure the corresponding contribution to the temperature field, defined by

$$\xi = \iint_{A_{cs}} q dx dz, \tag{30}$$

where A_{cs} denotes the cooling source area. For the specified cooling source function, substituting Eqs. (27)–(29) into Eq. (30) yields

$$\xi = Q_m r_x r_z (\pi/4 - 1/\pi), \tag{31}$$

which is the product of the temporary cooling rate, the longitudinal radius of the cooling source, the vertical radius of the cooling source, and a constant.

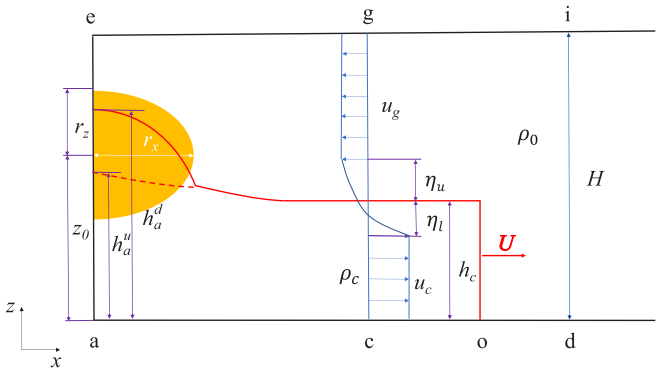

FIG. 8. A schematic of a cooling-source gravity current. A gravity current advances in the ambient with a front velocity of U, while the cooling source in the yellow area continuously supplies dense fluids. The red solid line represents the density interface and the red dashed line represents the longitudinal velocity interface.

The variation of the temperature T is correlated with the variation of the density ρ as

$$\frac{\rho - \rho_0}{\rho_0} = -\beta(T - T_0), \tag{32}$$

where β is the heat-expansion coefficient of the fluid. T_0 is the reference temperature, set to the value in the ambient for convenience. Thus, the source term in the density budget equation is calculated by

$$S_\rho = -\rho_0 \beta q, \tag{33}$$

and integrating it in the ellipsoidal cooling source area yields $-\rho_0\beta\xi$, which can evaluate the effect of the cooling source on the density field.

Figure 8 shows the configuration of a cooling-source gravity current. The viscous dissipation is assumed to be negligible in the cooling source region. The interfaces of the density and the longitudinal velocity are separated by the cooling source, based on the observation from direct numerical simulations in Sec. V. In the cooling source region, the mixing of density is neglected, and a velocity discontinuity is assumed between the flowing layers.

First, the density profile at ae is

$$\rho = \begin{cases} \rho_a, & 0 < z < h_a^d \\ \rho_0, & h_a^d < z < H, \end{cases} \tag{34}$$

where h_a^d is the depth of the dense fluid layer. The longitudinal velocity is simply 0 at ae, and the profile of its derivative with respect to the longitudinal coordinate can be obtained by integrating the mass budget equation along the vertical direction, i.e.,

$$u' = \begin{cases} u'_a, & 0 < z < h_a^u \\ -\left(u'_a h_a^u\right)/\left(H - h_a^u\right), & h_a^u < z < H, \end{cases} \tag{35}$$

where h_a^u is the height of the longitudinal velocity interface and u'_a is the derivative of the longitudinal velocity with respect to the longitudinal coordinate at the bottom boundary. An integration of the mass budget equation in the vertical direction, the boundary conditions, and substitution of Eq. (35) yields the vertical velocity profile

$$w = \begin{cases} -u'_a z, & 0 < z < h_a^u \\ -u'_a h_a^u + \left(u'_a h_a^u\right)\left(z - h_a^u\right)/\left(H - h_a^u\right), & h_a^u < z < H, \end{cases} \tag{36}$$

suggesting that the vertical velocity is related to the longitudinal gradient of the longitudinal velocity.

Since the vertical velocity cannot be ignored, the hydrostatic balance does not hold in the cooling source region. The vertical momentum budget equation along with the left boundary condition should be taken into account, i.e.,

$$\frac{1}{2}\frac{\partial ww}{\partial z} = -\frac{1}{\rho_0}\frac{\partial p}{\partial z} - \frac{\rho g}{\rho_0}. \tag{37}$$

The vertical integration of Eq. (37) and imposing the bottom boundary condition produce the pressure distribution

$$p = p_a - \frac{1}{2}\rho_0 w^2 - \int_0^z \rho g dz', \tag{38}$$

and substituting Eqs. (34) and (36) into it results in the final expression that is rather complicated. The pressure difference of *ae* is easily computed by taking the upper limit of the integral in Eq. (38) to be H, yielding

$$p_a = p_e + \rho_0 g\left(H - h_a^d\right) + \rho_a g h_a^d. \tag{39}$$

Along the bottom and top boundaries, the pressure differences can be evaluated by the application of the unsteady Bernoulli equations, i.e.,

$$p_i - p_e = -\rho_0 U u_g, \tag{40}$$

$$p_d - p_a = -\rho_c U u_c. \tag{41}$$

These pressure differences together with Eq. (11) should satisfy a single-value pressure field, i.e.,

$$-(\rho_a - \rho_0) g h_a^d + \rho_c U u_c - \rho_0 U u_g = 0. \tag{42}$$

Integrating the density budget equation in the control volume of *aedi* yields

$$U\left(\int_c^g \rho dz - \int_d^i \rho dz\right) = -\rho_0 \beta \xi, \tag{43}$$

implying that the cooling source is the density supply of the propagating front. The integration of the longitudinal momentum budget equation in the control volume of *aedi* results in

$$U\int_c^g \rho u dz - \int_a^e p dz + \int_d^i p dz = 0. \tag{44}$$

The assumption that the energy dissipation only occurs behind the front is adopted. Hence, the energy is assumed to be conserved in the control volume of *aecg*, yielding

$$\int_c^g \left(\frac{1}{2}\rho u^2 + p + \rho g z\right) u dz = -\rho_0 \beta \xi g z_0, \tag{45}$$

which suggests that the net energy flux at the front is equal to the energy contribution of the cooling source.

We will integrate the budget equations only in the vertical direction at *ae* to find out more relations at the left boundary of the cooling source region. The vertical integration of the density budget equation at *ae* along with the boundary conditions gives

$$\int_a^e \rho u' dz = -\frac{\gamma \rho_0 \beta \xi}{r_x}, \tag{46}$$

where

$$\gamma = \frac{\int_{-1}^{1} \cos^2\left(\frac{\pi}{2}\sqrt{z^2}\right) dz}{\int_0^1 \int_{-\sqrt{1-x^2}}^{\sqrt{1-x^2}} \cos^2\left(\frac{\pi}{2}\sqrt{x^2+z^2}\right) dz dx}. \tag{47}$$

Similar relationships can be deduced by integrating the energy budget equation in the vertical direction and utilizing the boundary conditions, i.e.,

$$\int_a^e (p + \rho g z) u' dz = -\frac{\gamma \rho_0 \beta \xi g z_0}{r_x}. \tag{48}$$

Integrating the longitudinal momentum budget equation in the vertical direction together with the boundary conditions yields

$$\int_a^e p' dz = 0, \tag{49}$$

where p' is the derivative of the pressure with respect to the longitudinal coordinate. Directly substituting Eq. (38) into Eq. (49) will invoke extra unknowns, so we approximate the derivative of the pressure with respect to the longitudinal coordinate with an average of the values at the top and bottom boundaries, i.e.,

$$\int_a^e p' dz \approx \int_a^e \frac{1}{2}(p'_a + p'_e) dz. \tag{50}$$

It is easy to find $p'_a = 0$ and $p'_e = 0$ that make Eq. (49) intrinsically hold, which does not provide any useful relations. The pressure Poisson equation can be utilized to consider the pressure compatibility at *ae*, written in a two-dimensional form as

$$\frac{\partial^2 p}{\partial x^2} + \frac{\partial^2 p}{\partial z^2} = -\rho_0 \left(\frac{\partial^2 uu}{\partial x^2} + \frac{\partial^2 ww}{\partial z^2} + 2\frac{\partial^2 uw}{\partial xz} \right) - \frac{\partial \rho}{\partial z} g. \tag{51}$$

Integrating Eq. (51) along the vertical direction in conjunction with the boundary conditions yields

$$\int_a^e (p'' + 2\rho u'^2) dz = 0, \tag{52}$$

where p'' denotes the second-order derivative of the pressure with respect to the longitudinal coordinate. Approximating it in a similar way results in

$$\int_a^e (p'' + 2\rho u'^2) dz \approx \int_a^e \left[\frac{1}{2}(p''_a + p''_e) + 2\rho u'^2 \right] dz, \tag{53}$$

where p''_a and p''_e are easy to calculate by

$$p''_a = -\rho_a u'^2_a, \; p''_e = -\rho_0 \left(\frac{h^u_a}{H - h^u_a} \right)^2 u'^2_a. \tag{54}$$

Finally, by adopting the Boussinesq approximation and numerically solving Eqs. (6), (7), (14), (15), (42)–(46), (48), and (53) with the Newton iterative method, the front characteristics are correlated with the thermodynamic and geometric properties of the cooling source.

The integral model suggests that the front depth could be determined by two geometric properties of the cooling source that are the center height and longitudinal radius of the cooling source. Thus, eliminating the geometric properties of the cooling source to obtain the front velocity as a function of the front depth is impossible. Results from the integral model for the cooling-source gravity current will be discussed in detail in Sec. V, and the feasibility will be assessed by direct numerical simulations as well.

V. DIRECT NUMERICAL SIMULATION OF THE COOLING-SOURCE GRAVITY CURRENT

A. Simulation setup

Direct numerical simulations will directly solve the governing equations nondimensionalized by the characteristic scales incorporating the properties of the cooling source, avoiding using the density difference which is not predefined for the cooling-source gravity current. We scale the length with respect to the channel height H, and a possible choice of the characteristic velocity scale is

$$U_c = (-\beta\xi g)^{1/3}. \tag{55}$$

The Reynolds number is defined by

$$\mathrm{Re} = \frac{U_c H}{\nu}. \tag{56}$$

We know that the Froude number is calculated by

$$\mathrm{Fr} = \frac{U}{\left(\frac{\rho_c-\rho_0}{\rho_0} g h_c\right)^{1/2}}, \tag{57}$$

and substituting Eq. (43) and (55) into it yields

$$\frac{U}{U_c} = \mathrm{Fr}^{2/3}, \tag{58}$$

which illustrates that the dimensionless front velocity is $2/3$ power of the Froude number if the dense fluids supplied by the cooling source are all used for the evolution of a front. The dimensionless density is computed from

$$\tilde{\rho} = \frac{(\rho - \rho_0)}{\rho_0(-\beta\xi)^{2/3} g^{-1/3} H^{-1}}, \tag{59}$$

where the wide tilde denotes the dimensionless quantity (we will not state again in the following). Finally, the dimensionless governing equations can be written as

$$\frac{\partial \tilde{u}_j}{\partial \tilde{x}_j} = 0, \tag{60}$$

$$\frac{\partial \tilde{u}_i}{\partial \tilde{t}} + \frac{\partial \tilde{u}_i \tilde{u}_j}{\partial \tilde{x}_j} = -\frac{\partial \tilde{p}}{\partial \tilde{x}_i} + \frac{1}{\mathrm{Re}} \frac{\partial^2 \tilde{u}_i}{\partial \tilde{x}_j \tilde{x}_j} + \tilde{\rho} e_i^g, \tag{61}$$

$$\frac{\partial \tilde{\rho}}{\partial \tilde{t}} + \frac{\partial \tilde{\rho} \tilde{u}_j}{\partial \tilde{x}_j} = \frac{1}{\mathrm{ReSc}} \frac{\partial^2 \tilde{\rho}}{\partial \tilde{x}_j \tilde{x}_j} - \tilde{q}, \tag{62}$$

where Sc is the Schmidt number that is the ratio of the kinematic viscosity and the molecular diffusion coefficient of the density field.

A description of the numerical method employed for the integration of the dimensionless governing equations is specified here. The present code uses a second-order accurate, central finite difference scheme on a staggered grid for spatial discretization. An explicit low-storage third-order Runge-Kutta time advancement is employed to evaluate spatial derivatives except the wall-normal diffusion term which is solved using the Crank-Nicholson technique to guarantee the computational stability. A fractional step method is adopted for the velocity-pressure decoupling of incompressible flows, which projects the velocity into a divergence-free space to satisfy the continuity equation. The pressure Poisson equation is transformed into the cosine series in the longitudinal direction, resulting in a tridiagonal system that can be solved easily and efficiently. The code is fully parallelized using the message passing interface communication standard.

A symmetry boundary condition is applied in the longitudinal direction. The top and bottom boundaries are slip. Homogeneous Neumann conditions for the density are applied at the bottom

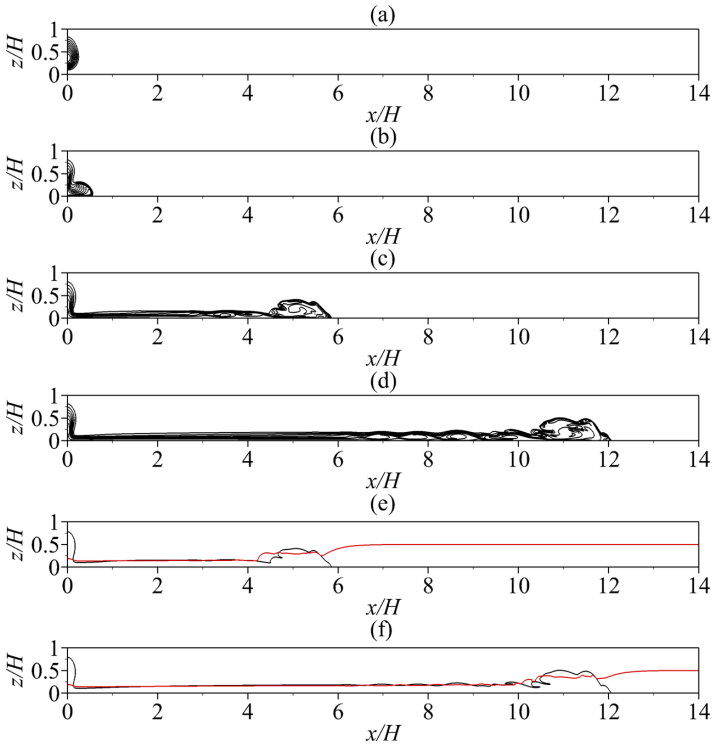

FIG. 9. The instantaneous fields of the density and the longitudinal velocity at various times from direct numerical simulations. The contour lines of the density evenly distributed between the minimum and maximum values at $\tilde{t} = 0.5$ (a), 1 (b), 5 (c), 10 (d). The isoline of the density that is 1/10 of the maximum value (black line) and the isoline of the zero longitudinal velocity (red line) at $\tilde{t} = 5$ (e), 10 (f).

and top of the domain. Simulations are started with zero uniform-distributed velocity and density fields. The computational box is the domain sketched in Fig. 8 with $\tilde{L}_x \times \tilde{L}_z = 16 \times 1$ for a two-dimensional simulation. The Schmidt number is set to the unit. We choose a high Reynolds number of 5000 and employ grid points of mesh as $N_x \times N_z = 3072 \times 192$. The time step is limited by the Courant-Friedrich-Lewy (CFL) condition to prevent the computation from oscillations. The overall dimensionless computational time is set to 10 to ensure that the flow undergoes a full sequence of phases and remains unaffected by the right boundary.

B. Results

The geometric parameters of the cooling source are set to $r_x/H = 0.3$, $r_z/H = 0.45$, and $z_0/H = 0.5$. The instantaneous fields of the density and the longitudinal velocity from direct numerical simulations are presented in Fig. 9. The development of the cooling-source gravity current is clearly demonstrated. A volume of cold air forms and descends gradually. The heavier fluid collides with the bottom boundary and propagates longitudinally in the ambient. The isolines are concentrated at the density interface, indicating a sharp density gradient. The vortex is generated by the Kelvin-Helmholtz instability at the density interface. As the gravity current moves further, it is visible that the turbulent structures of the front become more and more complex. In general, the cooling-source gravity current manifests the essential characteristics of a gravity current [28]. Moreover, in the cooling source region, the density interface resembling the upper boundary of the cooling source is at a higher position than the longitudinal velocity interface. The interfaces of the density and the longitudinal velocity tend to overlap in the area not influenced by the cooling source. The density

interface is smooth away from the head in the cooling source region, revealing minor turbulent mixing. At the front of the gravity current, turbulent mixing causes obvious undulations.

To quantitatively investigate the motion of the cooling-source gravity current, it is necessary to define the front velocity in a convenient way. Inspired by the unambiguous way to define a local depth of the gravity current [33,41,42], we adopt a new definition as

$$\tilde{h}(\tilde{x},\tilde{t}) = \frac{\int_0^1 \tilde{\rho}(\tilde{x},\tilde{z},\tilde{t})d\tilde{z}}{\tilde{\rho}^{\mathrm{ave}}(\tilde{t})}, \tag{63}$$

where $\tilde{\rho}^{\mathrm{ave}}(\tilde{t})$ is the spatial averaged density in the dense fluid roughly estimated by

$$\tilde{\rho}^{\mathrm{ave}}(\tilde{t}) = \frac{\iint_{S_a} \tilde{\rho}(\tilde{x},\tilde{z},\tilde{t})^2 d\tilde{x}d\tilde{z}}{\iint_{S_a} \tilde{\rho}(\tilde{x},\tilde{z},\tilde{t})d\tilde{x}d\tilde{z}}, \tag{64}$$

where S_a denotes the two-dimensional domain that does not include the cooling source region. The front position is theoretically where the local depth of the gravity current reduces to zero. Concerning diffusion and numerical noises, a small threshold is chosen, 10^{-3} in our simulations. The front velocity is simply the derivative of the front position with respect to time. The front depth is approximated by averaging the local depth of the gravity current along the longitudinal direction, i.e.,

$$\tilde{h}_c = \frac{\int_{\tilde{r}_x}^{\tilde{x}_n} \tilde{h}(\tilde{x},\tilde{t})d\tilde{x}}{\tilde{x}_n - \tilde{r}_x}. \tag{65}$$

The evolution and self-similar phases of the gravity currents initiated by releasing a volume of dense fluid have been widely studied in the literature. The lock-release gravity current goes through a steady propagation in the slumping phase after the acceleration, a decay in the inertial phase, and a more pronounced deceleration in the viscous phase [30,42]. The transition from the slumping phase to the inertial phase occurs when the reflected back-propagating wave catches up with the front [42]. The duration of the slumping phase has been found to be between three and ten lock lengths for an axisymmetric lock-release experiment [43]. The gravity current produced by an elevated thermal undergoes the initial acceleration phase and reaches the self-similar phase that resembles the inertial phase of an axisymmetric lock-release gravity current [15–18]. The transition from a thermal that has impacted on the ground to the self-similar phase of an axisymmetric gravity current is referred to as the slumping phase or the adjustment phase [17]. The duration of the adjustment phase depends on whether the vortex has been partially or fully formed in the thermal when impacting the ground [17].

Box models assuming that the gravity current evolves in the form of an area rectangle can provide an insight into the self-similar phases and the scaling laws [19–22]. Noting that the dense fluids are supplied by the cooling source, the box model predicts a steady advancing front under the inertial-buoyancy balance. By further supposing negligible entrainment, the box model predicts a slightly decaying propagation under the viscous-buoyancy balance. The details of implementing the box model are specified in Appendix A. Under the viscous-buoyancy balance, the front velocity scales as $-1/5$ power of time [Eq. (A21)], and the front depth scales as $1/5$ power of time [Eq. (A22)]. The time evolution of the dimensionless front velocity and the front depth shown in Fig. 10 reveals the phases of spreading of the cooling-source gravity current. During the acceleration phase ($\tilde{t} < 1$), a volume of dense fluid forms and descends, which also spreads along the longitudinal direction. The flow goes through an adjustment phase ($1 < \tilde{t} < 3$) after the descending fluid impacts with the bottom wall and before reaching the self-similar phase. A minor decline in the front velocity and an obvious decrease in the front depth are observed during the adjustment phase. The behavior of the adjustment phase is very interesting, but a comprehensive investigation of it is beyond the scope of this paper. The spreading of the gravity current maintains steady in the inertial phase ($3 < \tilde{t} < 6$) and slows down in the viscous phase ($\tilde{t} > 6$), both in good agreement with the box model.

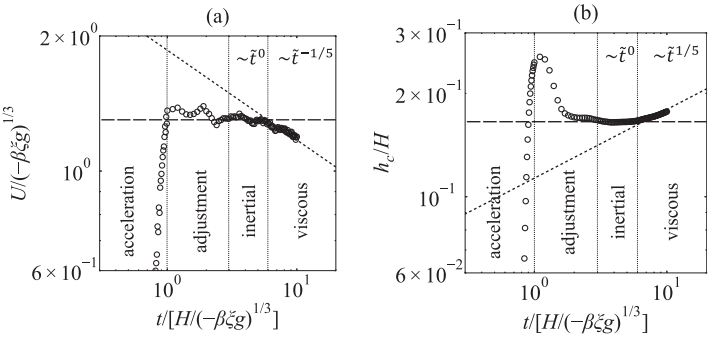

FIG. 10. The time evolution of the dimensionless front velocity (a) and the front depth (b) in a logarithmic scale. The symbols represent results from direct numerical simulations. The dashed lines are the scaling laws in the inertial phase predicted by the box model interpolated with the data at $3 < \tilde{t} < 6$. The dotted lines are the scaling laws in the viscous phase predicted by the box model interpolated with the data at $6 < \tilde{t} < 10$.

The integral model supposing a steady propagation is applicable for the inertial phase of a cooling-source gravity current. Therefore, we extract and average the front characteristics in the inertial phase to examine the influence of the geometric properties of the cooling source. For a clear definition of the inertial phase, the ratio of the inertial force and the viscous force in the dense fluid is calculated by

$$\frac{\tilde{f}_I}{\tilde{f}_V} = \frac{\int_{\tilde{r}_x}^{\tilde{x}_n}\int_0^{\tilde{h}}\left(\frac{\partial\tilde{u}\tilde{u}}{\partial\tilde{x}} + \frac{\partial\tilde{u}\tilde{w}}{\partial\tilde{z}}\right)d\tilde{z}d\tilde{x}}{\int_{\tilde{r}_x}^{\tilde{x}_n}\int_0^{\tilde{h}}\frac{1}{\mathrm{Re}}\left(\frac{\partial^2\tilde{u}}{\partial\tilde{x}^2} + \frac{\partial^2\tilde{u}}{\partial\tilde{z}^2}\right)d\tilde{z}d\tilde{x}}, \tag{66}$$

which is supposed to be not below 30 in the inertial phase. The criterion is empirical, but results do not show significant differences if it is within a reasonable range. The front position should be away from the cooling source to guarantee that the flow has reached a steady state. Owing to the difficulty of directly determining the lower velocity transition layer in numerical simulations, the mixing coefficient of the front is calculated by

$$\Phi_l = \frac{\int_{\tilde{x}_n-2}^{\tilde{x}_n-1}\int_0^{\tilde{h}}\frac{\tilde{u}-\tilde{u}_0}{\tilde{u}_1-\tilde{u}_0}d\tilde{z}d\tilde{x}}{\int_{\tilde{x}_n-2}^{\tilde{x}_n-1}\int_0^{\tilde{h}}d\tilde{z}d\tilde{x}}, \tag{67}$$

where $\tilde{u}_0$ denotes the longitudinal velocity at the bottom boundary and $\tilde{u}_1$ denotes the longitudinal velocity at the top boundary. The mixing coefficient is averaged along the longitudinal direction at the front.

The dimensionless front velocity, the front depth, the relative thickness of the lower velocity transition layer, and the mixing coefficient of the front as functions of the center height of the cooling source are presented in Fig. 11. As the center height of the cooling source increases, the dimensionless front velocity maintains a discernible growth for a small longitudinal radius of the cooling source and undergoes a slight decline and then a sharp rise for a large longitudinal radius of the cooling source. The front depth exhibits an increasing trend from zero and a descending trend back to zero with a growing center height of the cooling source, the peak value of which seems to be limited by the longitudinal radius of the cooling source. The relative thickness of the lower velocity transition layer manifests a rising tendency as the center height of the cooling source grows. To further explain the underlying mechanism, we will utilize the conclusion in Sec. II that the dimensionless front velocity, which is equal to $2/3$ power of the Froude number, is negatively correlated with the front depth and positively correlated with the relative thickness of the lower velocity transition layer. Therefore, for a small longitudinal radius of the cooling source, the

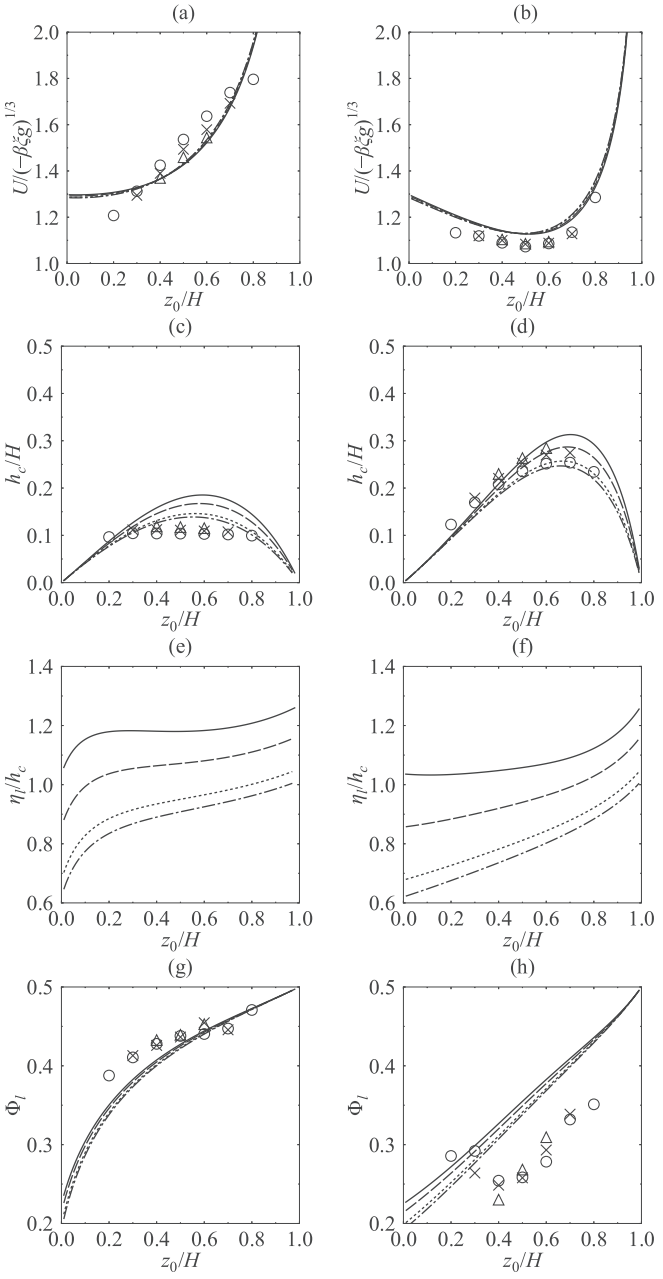

FIG. 11. The dimensionless front velocity [(a), (b)], the front depth [(c), (d)], the relative thickness of the lower velocity transition layer [(e), (f)], and the mixing coefficient of the front [(g), (h)] as functions of the center height of the cooling source for various longitudinal radiuses of the cooling source: $r_x/H = 0.2$ [(a), (c), (e), (g)] and $r_x/H = 0.6$ [(b), (d), (f), (h)]. The lines are predictions from the integral model assuming linear (solid line) and exponential velocity profiles with $\alpha = 1$ (dashed line), 3 (dotted line), 5 (dash-dotted line) in the transition layer. The symbols are results from direct numerical simulations: $r_z/H = 0.2$ (circle), $r_z/H = 0.3$ (cross), $r_z/H = 0.4$ (triangle).

variation of the front depth is relatively small and the thickened lower velocity transition layer plays a dominant role, leading to a monotonous growth of the dimensionless front velocity. For a large longitudinal radius of the cooling source, the influence of the substantially deeper dense fluid layer firstly overcomes that of the thickening lower velocity transition layer, resulting in a minor decrease in the dimensionless front velocity, and then the decaying front depth and the enhanced shear layer in the dense fluid both contribute to a significantly increasing dimensionless front velocity. The mixing coefficient of the front and the relative thickness of the lower velocity transition layer show similar trends. What's more, the mixing coefficient of the front can reach large values, demonstrating that the shear layer in the dense fluid could play a dominant role.

Figure 12 illustrates the mechanism that the longitudinal radius of the cooling source affects the dimensionless front velocity. As the longitudinal radius of the cooling source increases, the substantial decline in the dimensionless front velocity is attributed to the growing front depth and the diminishing shear layer in the dense fluid. The decreasing trend is more obvious for a higher center height of the cooling source, since the maximum front depth seems to be confined by the center height of the cooling source.

As displayed in Figs. 11 and 12, the dimensionless front velocity and the mixing coefficient are quite insensitive to the form of the velocity profile in the transition layer, which imposes an effect on the front depth and the relative thickness of the lower velocity transition layer. A linear velocity transition and an exponential velocity transition with $\alpha = 1, 3$ produce unphysical relative thicknesses of the lower velocity transition layer larger than 1, and an exponential velocity transition with $\alpha = 5$ is likely to be more reasonable for the cooling-source gravity current, revealing a rapid velocity transition from the bottom layer to the upper layer.

In the integral model, the vertical radius of the cooling source only incorporated in the areal integral of the cooling source function Eq. (31) that is used for nondimensionalization will not influence the dimensionless quantities, and its effect is confirmed to be very limited by direct numerical simulations. In general, the integral model provides a good prediction for the front velocity and the front depth. In terms of the mixing coefficient of the front, the integral model is qualitatively consistent with direct numerical simulations, and the quantitive error is possibly owing to the uncertainties in determining the interval of the longitudinal coordinate for the averaging procedure.

Obviously, the effect of the shear layer in the dense fluid, which is negligible in the lock-release gravity current, could be predominant in the cooling-source gravity current. Previous integral models not involving the shear layer in the dense fluid are incapable of forecasting this important characteristic of the cooling-source gravity current. A straightforward way of proving this is that almost the same front depth could correspond to quite different dimensionless front velocities as shown in Figs. 11(a) and 11(c), which is contradictory to the implication of previous integral models that the Froude number is entirely governed by the front depth. Figures 11 and 12 demonstrate that a small longitudinal radius and a large center height of the cooling source contribute to a high mixing coefficient. Hence, we infer that compared with instantaneously releasing a volume of dense fluid, an elevated cooling source that persistently supplies dense fluids probably brings about more mixing, resulting in a larger Froude number.

Oreskovic [14] invoked the Lundgren scaling approach [15] and found that it works well for the downburst outflow. They found that the time histories of the front positions normalized by the Lundgren scaling approach collapse for various geometric parameters of the cooling source. Here, we will examine the dependence of the front velocity normalized by the Lundgren scaling approach on the geometric properties of the cooling source. The data normalized by the Lundgren scaling approach for the full extent of the gravity currents is presented in Appendix B.

Oreskovic [14] defined the characteristic scales for an axisymmetric cooling source, and we will consider a two-dimensional case in a similar way. The characteristic length scale is defined by the equivalent radius of the cooling source, i.e.,

$$r_0 = (r_x r_z)^{\frac{1}{2}}. \tag{68}$$

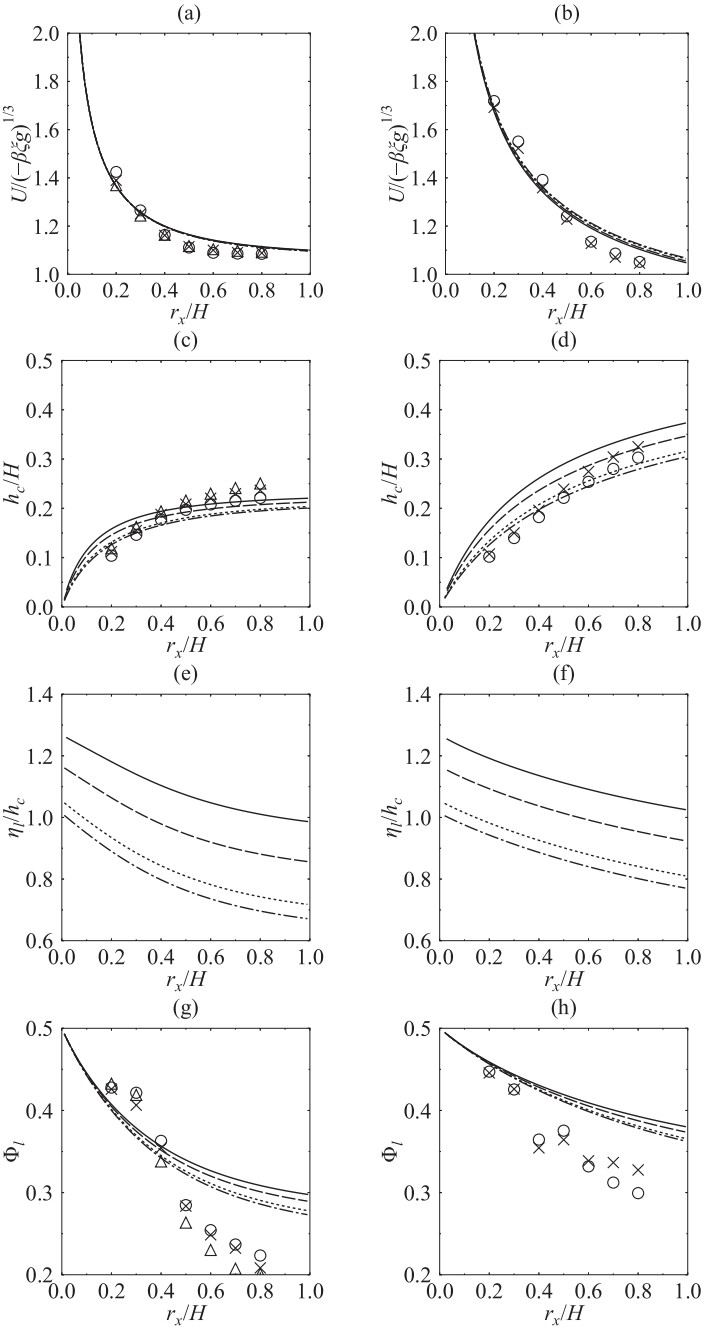

FIG. 12. The dimensionless front velocity [(a), (b)], the front depth [(c), (d)], the relative thickness of the lower velocity transition layer [(e), (f)], and the mixing coefficient of the front [(g), (h)] as functions of the longitudinal radius of the cooling source for various center heights of the cooling source: $z_0/H = 0.4$ [(a), (c), (e), (g)] and $z_0/H = 0.7$ [(b), (d), (f), (h)]. The lines are predictions from the integral model assuming linear (solid line) and exponential velocity profiles with $\alpha = 1$ (dashed line), 3 (dotted line), 5 (dash-dotted line) in the transition layer. The symbols are results from direct numerical simulations: $r_z/H = 0.2$ (circle), $r_z/H = 0.3$ (cross), $r_z/H = 0.4$ (triangle).

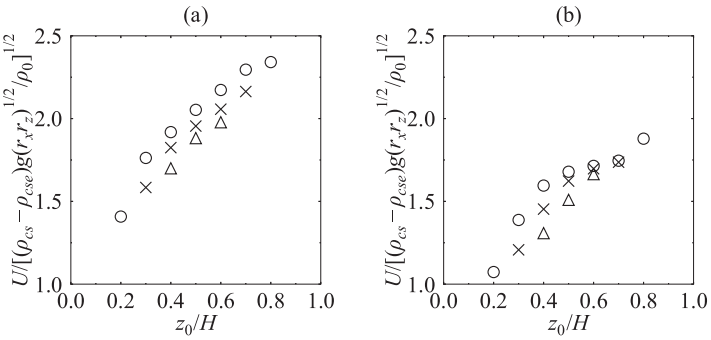

FIG. 13. The front velocity normalized by the Lundgren scaling approach [15] as a function of the center height of the cooling source for various longitudinal radiuses of the cooling source: $r_x/H = 0.2$ (a) and $r_x/H = 0.6$ (b). The symbols are results from direct numerical simulations: $r_z/H = 0.2$ (circle), $r_z/H = 0.3$ (cross), $r_z/H = 0.4$ (triangle).

The corresponding characteristic timescale is

$$t_0 = \left(\frac{r_0 \rho_{\mathrm{cse}}}{g(\rho_{\mathrm{cs}} - \rho_{\mathrm{cse}})}\right)^{\frac{1}{2}}, \tag{69}$$

where ρ_{cs} is the average density in the elliptic cooling source region, and ρ_{cse} is the mean density of the environment not included in the elliptic cooling source region. The characteristic velocity scale is then computed from

$$U_0 = \frac{r_0}{t_0} = \left(\frac{(\rho_{\mathrm{cs}} - \rho_{\mathrm{cse}})}{\rho_{\mathrm{cse}}} g (r_x r_z)^{\frac{1}{2}}\right)^{\frac{1}{2}}. \tag{70}$$

Thus, the dimensionless front velocity is calculated by

$$\frac{U}{U_0} = \frac{U}{\left(\frac{(\rho_{\mathrm{cs}}-\rho_{\mathrm{cse}})}{\rho_{\mathrm{cse}}} g (r_x r_z)^{\frac{1}{2}}\right)^{\frac{1}{2}}}, \tag{71}$$

and substituting Eq. (43) into it results in

$$\frac{U}{U_0} = \left(\frac{U}{(-\beta \xi g)^{\frac{1}{3}}}\right)^{\frac{3}{2}} \left(\frac{h_c}{H}\right)^{\frac{1}{2}} \left(\frac{r_x}{H}\frac{r_z}{H}\right)^{-\frac{1}{4}} \left(\frac{\rho_c - \rho_0}{\rho_{\mathrm{cs}} - \rho_{\mathrm{cse}}}\right)^{\frac{1}{2}} \left(\frac{\rho_{\mathrm{cse}}}{\rho_0}\right)^{\frac{1}{2}}, \tag{72}$$

which gives a transformation to the front velocity normalized by the Lundgren scaling approach. Applying the Boussinesq approximation yields

$$\frac{U}{U_0} = \left(\frac{U}{(-\beta \xi g)^{\frac{1}{3}}}\right)^{\frac{3}{2}} \left(\frac{h_c}{H}\right)^{\frac{1}{2}} \left(\frac{r_x}{H}\frac{r_z}{H}\right)^{-\frac{1}{4}} \left(\frac{\tilde{\rho}_c}{\tilde{\rho}_{\mathrm{cs}} - \tilde{\rho}_{\mathrm{cse}}}\right)^{\frac{1}{2}}, \tag{73}$$

where the ratio $\tilde{\rho}_c/(\tilde{\rho}_{\mathrm{cs}} - \tilde{\rho}_{\mathrm{cse}})$ can be directly computed from direct numerical simulations. As presented in Figs. 13 and 14, it is obvious that the front velocity normalized by the Lundgren scaling approach still exhibits an obvious reliance on the geometric properties of the cooling source. The rough conclusion of Oreskovic [14] is probably caused by a very narrow varying range of the geometric parameters and some coincidences, which is confirmed in Appendix B. Basically, there is no underlying mechanism, which can ensure that the scaling method for the gravity current produced by an elevated thermal is applicable for the cooling-source gravity current.

To explore the existence of a scaling approach that yields a dimensionless front velocity rarely relying on the geometric properties of the cooling source, we carefully examine the dimensionless

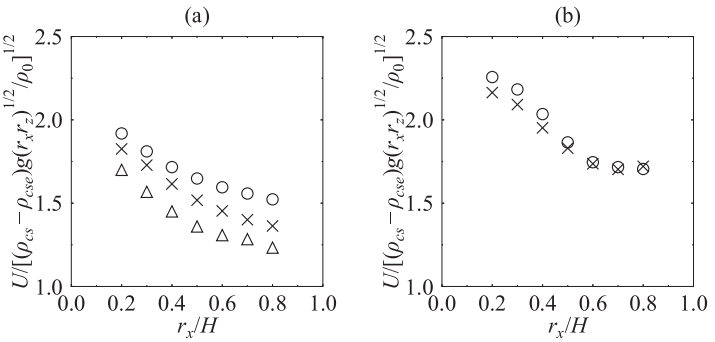

FIG. 14. The front velocity normalized by the Lundgren scaling approach [15] as a function of the longitudinal radius of the cooling source for various center heights of the cooling source: $z_0/H = 0.4$ (a) and $z_0/H = 0.7$ (b). The symbols are results from direct numerical simulations: $r_z/H = 0.2$ (circle), $r_z/H = 0.3$ (cross), $r_z/H = 0.4$ (triangle).

results of our scaling method. A possible choice of the characteristic velocity scale is

$$U_c^* = U_c\left(\frac{z_0}{h_c}\right)^{\frac{1}{3}} = \left(-\beta\xi g\frac{z_0}{h_c}\right)^{\frac{1}{3}}. \tag{74}$$

The corresponding dimensionless front velocity is given by

$$\frac{U}{U_c^*} = \frac{U}{\left(-\beta\xi g\frac{z_0}{h_c}\right)^{\frac{1}{3}}}, \tag{75}$$

and substituting Eq. (43) into it results in

$$\frac{U}{U_c^*} = \left(\frac{U}{\left(\frac{\rho_c-\rho_0}{\rho_0}gz_0\right)^{\frac{1}{2}}}\right)^{\frac{2}{3}}, \tag{76}$$

revealing an alternative choice of the characteristic velocity, i.e.,

$$U_c^{**} = \left(\frac{\rho_c-\rho_0}{\rho_0}gz_0\right)^{\frac{1}{2}}. \tag{77}$$

Thus, the corresponding dimensionless front velocity is the Froude number based on the center height of the cooling source, i.e.,

$$\frac{U}{U_c^{**}} = \frac{U}{\left(\frac{\rho_c-\rho_0}{\rho_0}gz_0\right)^{\frac{1}{2}}}, \tag{78}$$

and the transformation is

$$\frac{U}{U_c^{**}} = \left(\frac{U}{(-\beta\xi g)^{\frac{1}{3}}}\right)^{\frac{3}{2}}\left(\frac{h_c}{H}\right)^{\frac{1}{2}}\left(\frac{z_0}{H}\right)^{-\frac{1}{2}}. \tag{79}$$

The Froude number based on the center height of the cooling source as a function of the center height and longitudinal radius of the cooling source is shown in Figs. 15 and 16. The Froude number based on the center height of the cooling source almost maintains around unity and slightly relies on the geometric properties of the cooling source, indicating that the characteristic velocity given by Eq. (77) offers a good estimate of the front velocity for the cooling-source gravity current. The Froude number based on the center height of the cooling source demonstrates a discernible

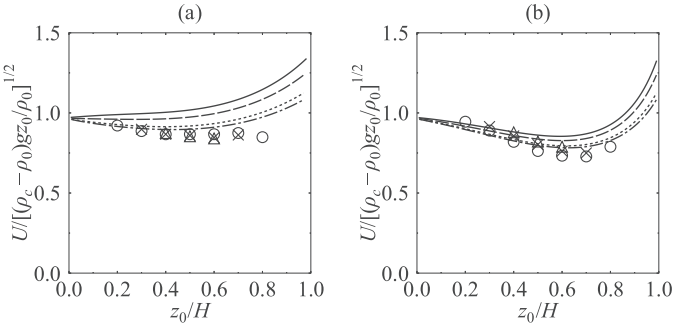

FIG. 15. The Froude number based on the center height of the cooling source as a function of the center height of the cooling source for various longitudinal radiuses of the cooling source: $r_x/H = 0.2$ (a) and $r_x/H = 0.6$ (b). The lines are predictions from the integral model assuming linear (solid line) and exponential velocity profiles with $\alpha = 1$ (dashed line), 3 (dotted line), 5 (dash-dotted line) in the transition layer. The symbols are results from direct numerical simulations: $r_z/H = 0.2$ (circle), $r_z/H = 0.3$ (cross), $r_z/H = 0.4$ (triangle).

dependence on the function of the velocity transition, and the most satisfactory agreement with the direct numerical simulations is found to be using the exponential profile with $\alpha = 5$.

Moreover, we will discuss the $H \to \infty$ limit, representing the gravity current propagating in an ambient fluid of infinite depth. $H \to \infty$ yields $z_0/H \to 0$ and $r_x/H \to 0$, and the remaining nondimensional geometric parameter is z_0/r_x. As presented in Fig. 17, the Froude number based on the center height of the cooling source seems to be entirely independent of the ratio of the center height and the longitudinal radius of the cooling source.

VI. CONCLUSIONS

In this paper, a unified integral model, incorporating a continuous velocity transition across the density interface, has been developed for the lock-release and cooling-source gravity currents. The general part of the integral model only concerning the front suggests that the Froude number is determined by the front depth and the relative thickness of the lower velocity transition layer. Introducing the shear layer in the dense fluid gives rise to a larger Froude number, and a mixing

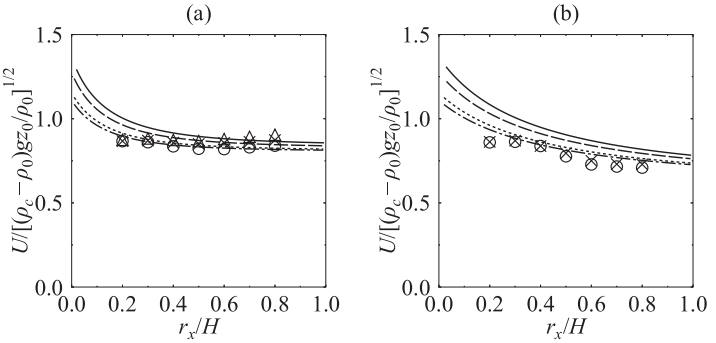

FIG. 16. The Froude number based on the center height of the cooling source as a function of the longitudinal radius of the cooling source for various center heights of the cooling source: $z_0/H = 0.4$ (a) and $z_0/H = 0.7$ (b). The lines are predictions from the integral model assuming linear (solid line) and exponential velocity profiles with $\alpha = 1$ (dashed line), 3 (dotted line), 5 (dash-dotted line) in the transition layer. The symbols are results from direct numerical simulations: $r_z/H = 0.2$ (circle), $r_z/H = 0.3$ (cross), $r_z/H = 0.4$ (triangle).

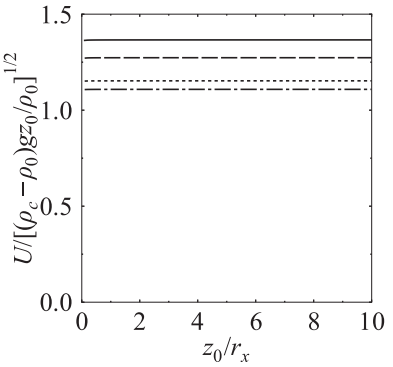

FIG. 17. The Froude number based on the center height of the cooling source as a function of the ratio of the center height and longitudinal radius of the cooling source as $H \to \infty$. The lines are predictions from the integral model assuming linear (solid line) and exponential velocity profiles with $\alpha = 1$ (dashed line), 3 (dotted line), 5 (dash-dotted line) in the transition layer.

coefficient is defined to assess this effect, unifying results with different velocity transitions. For the lock-release gravity current, the Froude number as a function of the front depth predicted by the integral model almost coincides with that from the vortex-wake model [38] that only includes the velocity transition in the ambient, revealing that the effect of the shear layer in the dense fluid is negligible. The front features are also related with the lock depth, and a slightly improved prediction is provided by the integral model. The integral model for the cooling-source gravity current correlates the front characteristics with the thermodynamic and geometric properties of the cooling source.

Direct numerical simulations of the cooling-source gravity current have been performed to assess the applicability of the integral model. The interfacial vortex induced by the Kelvin-Helmholtz instability is clearly seen in the instantaneous fields, and the cooling-source gravity current manifests the common features of a gravity current. The phases of spreading have been well captured. A volume of heavier fluid forms and descends, colliding with the bottom boundary to generate a front longitudinally evolving in the ambient. After an adjustment, the advancing front tends to be stable during the inertial phase and decelerates gradually as the viscous force becomes dominant. During the self-similar phases, the fitted scaling laws are in good agreement with the prediction from the box model. The integral model has been confirmed to offer a good estimate of the dimensionless front velocity and the front depth during the inertial phase. It is revealed by the theory and simulations that the center height and the longitudinal radius of the cooling source jointly determine the dimensionless front velocity and the front depth, both of which are quite insensitive to the vertical radius of the cooling source. Results also indicate that previous integral models ignoring the lower velocity transition layer are not able to capture the important characteristic of the cooling-source gravity current that the shear layer in the dense fluid could be predominant. The front velocity normalized by the Lundgren scaling approach exhibits a strong dependence on the geometric properties of the cooling source. Furthermore, we have found that the Froude number based on the center height of the cooling source rarely depends on the geometric properties of the cooling source.

The integral model for the cooling-source gravity current only allows the energy dissipation at the front of the gravity current, and the energy conservation still remains in the formulation. Therefore, efforts could be made to eliminate energy arguments by future research. The density interface is assumed to be infinitely thin owing to the numerical complexity of involving the mixing of density, the effect of which has been investigated in the lock-release gravity current [36,44] and the internal bores [45], and measured in a continuous gravity current [46]. Nevertheless, determining the thickness of the mixing layer in the integral model is quite challenging. What's

more, the box model also ignores the entrainment of ambient fluid during the self-similar phases of the cooling-source gravity current, which needs to be considered by future studies. Shallow water models supposing that the longitudinal length scale is substantially larger than the depth and allowing longitudinal variations in the interior of the gravity current [23–25] can be introduced to explore the cooling-source gravity current in future. The two-layer shallow-water model has been successfully employed to study the sustained gravity currents [47]. Based on the investigation in this paper, the shear layer should be taken into account in establishing a shallow-water theory for the cooling-source gravity current. In addition, correlating the inflow boundary condition of the shallow-water equations with the thermodynamic and geometric properties of the cooling source is crucial, since the hydrostatic balance is not justified in the cooling source region.

Bond and Johari [48], Lai *et al.* [49], and Kruger [17] established models for the initial stages of releasing an elevated thermal, which can be split into three phases: the draining phase, the development phase, and the self-similar thermal phase. Kruger [17] has found that the transition from a thermal to an axisymmetric gravity current, i.e., the adjustment phase, depends on the phase of the thermal at the time of impact, affected by the geometry of the thermal. After impacting the ground, the front velocity and the depth of the gravity current both increase in the case of a thermal in the draining phase or development phase, and a small decrease in the depth of the gravity current and a slight change in the front velocity have been observed in the case of the self-similar thermal. A better understanding of the acceleration phase and the adjustment phase of the cooling-source gravity current is required, since it may be different from the gravity current generated by an elevated thermal.

ACKNOWLEDGMENTS

Financial supports by grants from the National Natural Science Foundation of China (Grants No. 92052202, No. 11972175, and No. 11490553) are gratefully acknowledged.

APPENDIX A: THE BOX MODEL FOR THE COOLING-SOURCE GRAVITY CURRENT

The box model will be employed to predict a sequence of self-similar phases and the scaling laws for the cooling-source gravity current. The implication of the box model is that the gravity current evolves as an area rectangle with changing volume in time [19–22]. Thus, the propagation is assumed to be with time t at some power, i.e.,

$$h_n x_n = \mathcal{V} t^{\omega_\mathcal{V}}, \tag{A1}$$

where x_n is the front position and h_n is the depth of the gravity current. $\omega_\mathcal{V}$ is a dimensionless non-negative constant and $\mathcal{V}$ is a positive constant, the dimension of which is $\mathrm{m}^2\mathrm{s}^{-\omega_\mathcal{V}}$. We suppose a similar behavior of the front position as

$$x_n = \mathcal{X} t^{\omega_\mathcal{X}}, \tag{A2}$$

the derivative of which with respect to time is

$$U = \omega_\mathcal{X} \mathcal{X} t^{\omega_\mathcal{X} - 1}, \tag{A3}$$

where U denotes the front velocity. The dimension of the positive constant $\mathcal{X}$ is $\mathrm{ms}^{-\omega_\mathcal{X}}$, and $\omega_\mathcal{X}$ is a dimensionless constant. Substituting Eq. (A2) into Eq. (A1) yields

$$h_n = \frac{\mathcal{V}}{\mathcal{X}} t^{\omega_\mathcal{V} - \omega_\mathcal{X}}. \tag{A4}$$

Concerning that the density is supplied by the cooling source results in

$$(\rho_n - \rho_0) h_n x_n = -\rho_0 \beta \xi t, \tag{A5}$$

where ρ_n is the density within the gravity current. Substituting Eq. (A1) into Eq. (A5) yields

$$(\rho_n - \rho_0) = \frac{-\rho_0 \beta \xi}{\mathcal{V}} t^{1-\omega_\mathcal{V}}. \tag{A6}$$

The total buoyancy force f_B, the total inertial force f_I, and the total viscous f_V force within the gravity current can be calculated, and substituting Eqs. (A2)–(A4) and (A6) into them yields

$$f_B = \frac{1}{2}(\rho_n - \rho_0) h_n^2 g = -\frac{\rho_0 \beta \xi g \mathcal{V}}{2\mathcal{X}^2} t^{\omega_\mathcal{V} - 2\omega_\mathcal{X} + 1}, \tag{A7}$$

$$f_I = \frac{1}{2}\rho_0 U^2 h_n = \frac{\rho_0 \mathcal{V} \mathcal{X} \omega_\mathcal{X}^2}{2} t^{\omega_\mathcal{V} + \omega_\mathcal{X} - 2}, \tag{A8}$$

$$f_V = \frac{1}{2}\frac{\rho_0 \nu U x_n}{h_n} = \frac{\rho_0 \nu \mathcal{X}^3 \omega_\mathcal{X}}{2\mathcal{V}} t^{-\omega_\mathcal{V} + 3\omega_\mathcal{X} - 1}. \tag{A9}$$

The propagation of an inertial gravity current is governed by the jump condition at the nose, i.e.,

$$U = \mathrm{Fr}\left(\frac{(\rho_n - \rho_0) g h_n}{\rho_0}\right)^{1/2}, \tag{A10}$$

and substitution of Eq. (A3), (A4), and (A6) into it yields

$$\mathcal{X} = \mathrm{Fr}^{2/3}(-\beta \xi g)^{1/3}, \tag{A11}$$

$$\omega_\mathcal{X} = 1. \tag{A12}$$

Therefore, we find a steady-state advancing front under the inertial-buoyancy balance, i.e.,

$$x_n = \mathrm{Fr}^{2/3}(-\beta \xi g)^{1/3} t, \tag{A13}$$

$$U = \mathrm{Fr}^{2/3}(-\beta \xi g)^{1/3}. \tag{A14}$$

Under the inertial-buoyancy balance, the front velocity undergoes a slight decline of $-1/3$ and $-1/2$ power of time for the two-dimensional and axisymmetric lock-release gravity currents, respectively, which has been comprehensively understood in previous studies [42]. The product of the density difference and the depth of the gravity current should satisfy

$$(\rho_n - \rho_0) h_n = \frac{\rho_0 (-\beta \xi)^{2/3}}{\mathrm{Fr}^{2/3} g^{1/3}}, \tag{A15}$$

and neglecting the entrainment gives a constant mass filling rate, i.e., $\omega_\mathcal{V} = 1$, which yields

$$(\rho_n - \rho_0) = \frac{-\rho_0 \beta \xi}{\mathcal{V}}, \tag{A16}$$

$$h_n = \frac{\mathcal{V}}{\mathrm{Fr}^{2/3}(-\beta \xi g)^{1/3}}. \tag{A17}$$

The viscous-buoyancy balance implies that the inertial force is negligible, and the buoyancy force is counteracted by the viscous force. Hence, equating Eqs. (A7) and (A9) yields

$$\frac{\mathcal{X}^5}{\mathcal{V}^2} = -\frac{\beta \xi g}{\nu \omega_\mathcal{X}}, \tag{A18}$$

$$5\omega_\mathcal{X} - 2\omega_\mathcal{V} - 2 = 0. \tag{A19}$$

TABLE I. A summary of the geometric parameters of the cooling source studied by Oreskovic [14] and the corresponding nondimensional parameters.

Case	H	z_0	r_x	r_z	z_0/H	r_x/H	r_z/H
Oreskovic1	4000m	2000m	1200m	1800m	0.5	0.3	0.45
Oreskovic2	4000m	1333m	800m	1200m	0.33325	0.2	0.3
Oreskovic3	4000m	1666m	1000m	1500m	0.4165	0.25	0.375

Assuming that the entrainment is negligible leads to a slightly decaying propagation

$$x_n = \left(\frac{4}{5}\right)^{-1/5} \mathcal{V}^{2/5} \left(\frac{-\beta\xi g}{\nu}\right)^{1/5} t^{4/5}, \tag{A20}$$

$$U = \left(\frac{4}{5}\right)^{3/5} \mathcal{V}^{2/5} \left(\frac{-\beta\xi g}{\nu}\right)^{1/5} t^{-1/5}, \tag{A21}$$

$$h_n = \left(\frac{4}{5}\right)^{1/5} \mathcal{V}^{3/5} \left(\frac{\nu}{-\beta\xi g}\right)^{1/5} t^{1/5}. \tag{A22}$$

The descending front velocity of the cooling-source gravity current is with $-1/5$ power of time under the viscous-buoyancy balance, which of the two-dimensional and axisymmetric lock-release gravity currents are with $-4/5$ and $-7/8$ power of time, respectively [42]. In addition, the ratio of the inertial force and the viscous force is evaluated by

$$\frac{f_I}{f_V} = \left(\frac{4}{5}\right)^{7/5} \frac{\mathcal{V}^{6/5}}{\nu} \left(\frac{\nu}{-\beta\xi g}\right)^{2/5} t^{-3/5}, \tag{A23}$$

revealing that the influence of the viscous force compared with the inertial force becomes more and more predominant.

APPENDIX B: THE TIME HISTORIES OF THE FRONT POSITIONS NORMALIZED BY DIFFERENT SCALING APPROACHES

Oreskovic [14] adopted the Lundgren scaling approach [15] to normalize the time histories of the front positions, which seem to collapse well for the downburst outflows. Table I displays a summary of the geometric parameters of the cooling source studied by Oreskovic [14] and the corresponding nondimensional parameters that are key for our study are also presented.

We do not directly compare our two-dimensional direct simulation results with Oreskovic [14], since they considered an axisymmetric gravity current. Instead, we will examine the normalized time histories of the front positions to see whether they can collapse. Figure 18 shows the time evolution of the front positions normalized by the Lundgren scaling approach for the geometric parameters of the cooling source summarized in Table I. The data collapse reasonably well, with a very slight deviation, which is consistent with Oreskovic [14].

To further testify the applicability of the Lundgren scaling method, a wide range of geometric parameters of the cooling source are investigated, presented in Fig. 19. The time histories between simulations with various center heights and vertical radiuses of the cooling source show obvious offsets, and the deviation is relatively small for the same center height of the cooling source. The similarity solution for the axisymmetric gravity current produced by an elevated thermal [16,17,50] unifies the Lundgren scaling approach. We will try to figure out why the Lundgren scaling approach is not applicable for the cooling-source gravity current through deriving the similarity solution for the two-dimensional gravity current generated by an elevated thermal. The buoyancy is assumed to

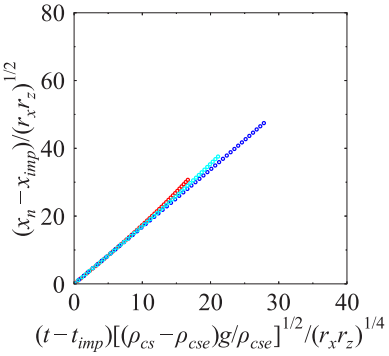

FIG. 18. The time evolution of the front positions normalized by the Lundgren scaling approach for the geometric parameters of the cooling source studied by Oreskovic [14]: Oreskovic1 (red), Oreskovic2 (blue), Oreskovic3 (cyan).

be conserved, i.e.,

$$g'V = g'_0 V_0, \tag{B1}$$

where g' is the reduced gravity, and V is the volume of the gravity current. The subscript 0 denotes the initial values. The box model assumes that the gravity current evolves as an area rectangle, yielding

$$V = x_n h_n. \tag{B2}$$

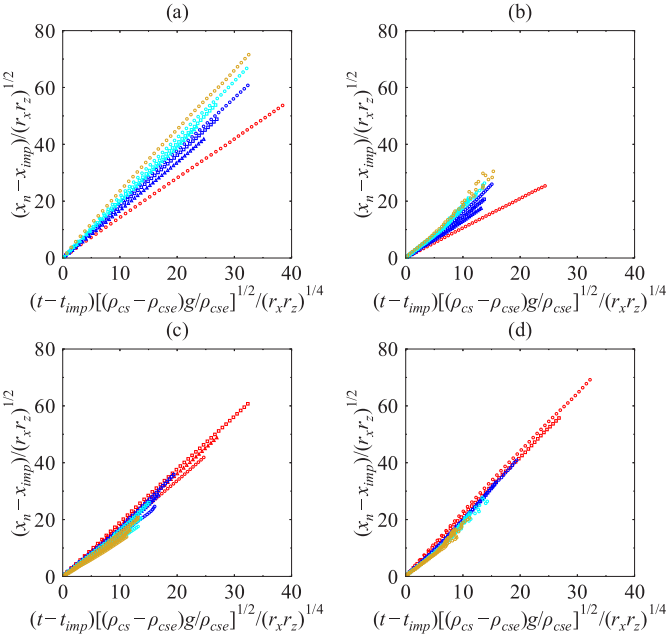

FIG. 19. The time evolution of the front positions normalized by the Lundgren scaling approach for various geometric parameters of the cooling source. (a) $r_x = 0.2$, (b) $r_x = 0.6$, (c) $z_0 = 0.4$, (d) $z_0 = 0.7$. In (a) and (b), $z_0 = 0.2$ (red), $z_0 = 0.4$ (blue), $z_0 = 0.6$ (cyan), $z_0 = 0.8$ (goldenrod). In (c) and (d), $r_x = 0.2$ (red), $r_x = 0.4$ (blue), $r_x = 0.6$ (cyan), $r_x = 0.8$ (goldenrod). In (a)–(d), $r_z = 0.2$ (circle), $r_z = 0.3$ (square), $r_z = 0.4$ (triangle).

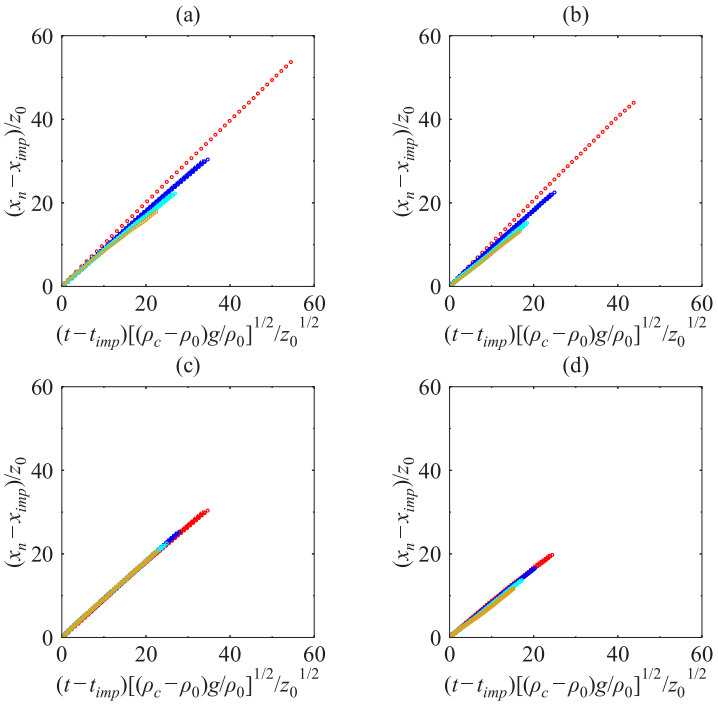

FIG. 20. The time evolution of the front positions normalized by the scaling approach for various geometric parameters of the cooling source. (a) $r_x = 0.2$, (b) $r_x = 0.6$, (c) $z_0 = 0.4$, (d) $z_0 = 0.7$. In (a) and (b), $z_0 = 0.2$ (red), $z_0 = 0.4$ (blue), $z_0 = 0.6$ (cyan), $z_0 = 0.8$ (goldenrod). In (c) and (d), $r_x = 0.2$ (red), $r_x = 0.4$ (blue), $r_x = 0.6$ (cyan), $r_x = 0.8$ (goldenrod). In (a)–(d), $r_z = 0.2$ (circle), $r_z = 0.3$ (square), $r_z = 0.4$ (triangle).

For an inertial gravity current, the jump condition at the nose is applied, i.e.,

$$U = \mathrm{Fr}(g' h_n)^{1/2}. \tag{B3}$$

Substituting Eqs. (B2) and (B3) into Eq. (B1) yields

$$U = \mathrm{Fr} {B_0}^{1/2} {x_n}^{-1/2}, \tag{B4}$$

where $B_0 = g'_0 V_0$. Noting that $U = dx_n/dt$ and integrating Eq. (B4) with respect to time result in

$${x_n}^{3/2} - {x_{\mathrm{imp}}}^{3/2} = \tfrac{3}{2}\mathrm{Fr} {B_0}^{1/2}(t - t_{\mathrm{imp}}), \tag{B5}$$

where x_{imp} is the front position at the impact, and t_{imp} is the time at the impact. For $x_n \gg x_{\mathrm{imp}}$, the front position at the impact becomes negligible, yielding

$$x_n = \left(\tfrac{3}{2}\mathrm{Fr} {B_0}^{1/2}\right)^{2/3}(t - t_{\mathrm{imp}})^{2/3}, \tag{B6}$$

and dividing it by the equivalent radius r_0 leads to

$$\frac{x_n}{r_0} = \left(\frac{3}{2}\mathrm{Fr}\right)^{2/3}\left(\frac{t - t_{\mathrm{imp}}}{{r_0}^{3/2} {B_0}^{-1/2}}\right)^{2/3}. \tag{B7}$$

For a half elliptic thermal, Eq. (B7) can be written as

$$\frac{x_n}{r_0} = \left(\frac{3}{2}\mathrm{Fr}\right)^{2/3}\left(\frac{\pi}{2}\right)^{1/3}\left(\frac{(t - t_{\mathrm{imp}}) {g'_0}^{1/2}}{{r_0}^{1/2}}\right)^{2/3}. \tag{B8}$$

It is assumed that the Froude number of the lock-release gravity current is constant in the range of 1–1.2 by Huq [50] and 1.4 by Rooney [16] and Kruger [17], which has also been investigated by the integral model in Sec. III. Hence, for the gravity currents produced by an elevated thermal with various geometries, the time histories of the front positions can collapse theoretically. However, we have found that the Froude number shows a strong dependence on the geometric parameters of the elevated cooling source in Sec. V. Moreover, when applying the Lundgren scaling approach to the cooling-source gravity current, the reduced gravity is taken as

$$g_0' = \frac{(\rho_{cs} - \rho_{cse})}{\rho_{cse}} g, \tag{B9}$$

where ρ_{cs} is the temporary density in the elliptic cooling source and ρ_{cse} is the temporary density of the environment not included in the elliptic cooling source. We note that g_0' represents the initial reduced gravity in the derivation of the similarity solution. Thus, there is a mismatch between the physical interpretation of g_0' in deducing the similarity solution and applying it to the gravity current produced by an elevated cooling source. Fundamentally, there is no underlying mechanism, which can guarantee that the scaling method for the gravity current produced by an elevated thermal is applicable for the cooling-source gravity current.

In Sec. V, the dependence of the Froude number based on the center height of the cooling source on the geometric parameters of the cooling source has been found to be relatively minor, so a different scaling method could be proposed. The characteristic length scale can be the center height of the cooling source, and the characteristic velocity scale is defined by Eq. (77). Figure 20 displays the time evolution of the front positions normalized by this scaling method. The data matches reasonably well with slight offsets between simulations with various center heights and vertical radiuses of the cooling source. For the same vertical height of the cooling source, the data perfectly collapse.

[1] I. Aoki, Y. Kurosaki, R. Osada, T. Sato, and F. Kimura, Dust storms generated by mesoscale cold fronts in the Tarim Basin, Northwest China, Geophys. Res. Lett. **32**, 6 (2005).

[2] S. Solomos, G. Kallos, E. Mavromatidis, and J. Kushta, Density currents as a desert dust mobilization mechanism, Atmos. Chem. Phys. **12**, 11199 (2012).

[3] A. Vukovic, M. Vujadinovic, G. Pejanovic, J. Andric, M. Kumjian, V. Djurdjevic, M. Dacic, A. K. Prasad, H. El-Askary, B. Paris *et al.*, Numerical simulation of "an American haboob," Atmos. Chem. Phys. **14**, 3211 (2014).

[4] N. D. Desouza, R. Kurchania, and M. S. Qureshi, Initiation of a convective dust storm over north India on 21 April 2010 inferred using satellite data, Meteorol. Atmos. Phys. **122**, 47 (2013).

[5] E. Meiburg, S. Radhakrishnan, and M. Nasr-Azadani, Modeling gravity and turbidity currents: Computational approaches and challenges, Appl. Mech. Rev. **67**, 040802 (2015).

[6] F. Pantillon, P. Knippertz, J. H. Marsham, and C. E. Birch, A parameterization of convective dust storms for models with mass-flux convection schemes, J. Atmos. Sci. **72**, 2545 (2015).

[7] L.-S. Zhang, J.-J. Tao, G.-H. Wang, and X.-J. Zheng, Experimental study on the origin of lobe-cleft structures in a sand storm, Acta Mech. Sin. **37**, 47 (2021).

[8] J. Anderson, L. Orf, and J. Straka, A 3-D model system for simulating thunderstorm microburst outflows, Meteorol. Atmos. Phys. **49**, 125 (1992).

[9] L. G. Orf, J. R. Anderson, and J. M. Straka, A three-dimensional numerical analysis of colliding microburst outflow dynamics, J. Atmos. Sci. **53**, 2490 (1996).

[10] W. Lin, L. Orf, E. Savory, and C. Novacco, Proposed large-scale modelling of the transient features of a downburst outflow, Wind. Struct. **10**, 315 (2007).

[11] M. S. Mason, G. S. Wood, and D. F. Fletcher, Numerical simulation of downburst winds, J. Wind Eng. Ind. Aerodyn. **97**, 523 (2009).

[12] B. C. Vermeire, L. G. Orf, and E. Savory, Improved modelling of downburst outflows for wind engineering applications using a cooling source approach, J. Wind Eng. Ind. Aerodyn. **99**, 801 (2011).
[13] L. G. Orf, C. Oreskovic, E. Savory, and E. Kantor, Circumferential analysis of a simulated three-dimensional downburst-producing thunderstorm outflow, J. Wind Eng. Ind. Aerodyn. **135**, 182 (2014).
[14] C. Oreskovic, Numerical Investigation of Full Scale Thunderstorm Downbursts: A Parametric Study and Comparison to Meteorological Model, master's thesis, The University of Western Ontario, 2016.
[15] T. Lundgren, J. Yao, and N. Mansour, Microburst modelling and scaling, J. Fluid Mech. **239**, 461 (1992).
[16] G. Rooney, Descent and spread of negatively buoyant thermals, J. Fluid Mech. **780**, 457 (2015).
[17] E. Kruger, Dynamics of Downdraughts and Cold Pools: An Experimental and Numerical Study, Ph.D. thesis, University of Cambridge, 2019
[18] S. Williams, Descent and Near-Surface Evolution of Atmospheric Downdraughts, Ph.D. thesis, University of Leeds, 2020.
[19] M. Ungarish, *An Introduction to Gravity Currents and Intrusions* (CRC Press, Boca Raton, FL, 2009).
[20] H. E. Huppert and J. E. Simpson, The slumping of gravity currents, J. Fluid Mech. **99**, 785 (1980).
[21] N. Didden and T. Maxworthy, The viscous spreading of plane and axisymmetric gravity currents, J. Fluid Mech. **121**, 27 (1982).
[22] H. E. Huppert, The propagation of two-dimensional and axisymmetric viscous gravity currents over a rigid horizontal surface, J. Fluid Mech. **121**, 43 (1982).
[23] J. W. Rottman and J. E. Simpson, Gravity currents produced by instantaneous releases of a heavy fluid in a rectangular channel, J. Fluid Mech. **135**, 95 (1983).
[24] C. G. Johnson and A. J. Hogg, Entraining gravity currents, J. Fluid Mech. **731**, 477 (2013).
[25] J. Kowalski and J. N. McElwaine, Shallow two-component gravity-driven flows with vertical variation, J. Fluid Mech. **714**, 434 (2013).
[26] C. Härtel, L. Kleiser, M. Michaud, and C. Stein, A direct numerical simulation approach to the study of intrusion fronts, J. Eng. Math. **32**, 103 (1997).
[27] C. Härtel, F. Carlsson, and M. Thunblom, Analysis and direct numerical simulation of the flow at a gravity-current head. Part 2. The lobe-and-cleft instability, J. Fluid Mech. **418**, 213 (2000).
[28] C. Härtel, E. Meiburg, and F. Necker, Analysis and direct numerical simulation of the flow at a gravity-current head. Part 1. Flow topology and front speed for slip and no-slip boundaries, J. Fluid Mech. **418**, 189 (2000).
[29] S. K. Ooi, G. Constantinescu, and L. Weber, Numerical simulations of lock-exchange compositional gravity current, J. Fluid Mech. **635**, 361 (2009).
[30] M. I. Cantero, S. Balachandar, M. H. García, and D. Bock, Turbulent structures in planar gravity currents and their influence on the flow dynamics, J. Geophys. Res. **113**, C8 (2008).
[31] T. von Kármán, The engineer grapples with nonlinear problems, Bull. Am. Math. Soc. **46**, 615 (1940).
[32] T. B. Benjamin, Gravity currents and related phenomena, J. Fluid Mech. **31**, 209 (1968).
[33] J. O. Shin, S. B. Dalziel, and P. F. Linden, Gravity currents produced by lock exchange, J. Fluid Mech. **521**, 1 (2004).
[34] M. Ungarish, Energy balances and front speed conditions of two-layer models for gravity currents produced by lock release, Acta Mech. **201**, 63 (2008).
[35] M. Ungarish, Energy balances for gravity currents with a jump at the interface produced by lock release, Acta Mech. **211**, 1 (2010).
[36] Z. Borden and E. Meiburg, Circulation based models for Boussinesq gravity currents, Phys. Fluids **25**, 101301 (2013).
[37] N. A. Konopliv, S. Smith, J. N. Mcelwaine, and E. Meiburg, Modelling gravity currents without an energy closure, J. Fluid Mech. **789**, 806 (2016).
[38] M. Ungarish and A. J. Hogg, Models of internal jumps and the fronts of gravity currents: Unifying two-layer theories and deriving new results, J. Fluid Mech. **846**, 654 (2018).
[39] J. B. Klemp, R. Rotunno, and W. C. Skamarock, On the dynamics of gravity currents in a channel, J. Fluid Mech. **269**, 169 (1994).
[40] B. Gebhart, Y. Jaluria, R. L. Mahajan, and B. S. Sammakia, *Buoyancy-Induced Flows and Transport* (Hemisphere, New York, 1988).

[41] B. Marino, L. Thomas, and P. Linden, The front condition for gravity currents, J. Fluid Mech. **536**, 49 (2005).
[42] M. I. Cantero, J. R. Lee, S. Balachandar, and M. H. Garcia, On the front velocity of gravity currents, J. Fluid Mech. **586**, 1 (2007).
[43] H. E. Huppert, Gravity currents: a personal perspective, J. Fluid Mech. **554**, 299 (2006).
[44] D. Sher and A. W. Woods, Gravity currents: entrainment, stratification and self-similarity, J. Fluid Mech. **784**, 130 (2015).
[45] Z. Borden and E. Meiburg, Circulation-based models for Boussinesq internal bores, J. Fluid Mech. **726**, R1 (2013).
[46] D. Sher and A. W. Woods, Mixing in continuous gravity currents, J. Fluid Mech. **818**, R4 (2017).
[47] A. J. Hogg, M. M. Nasr-Azadani, M. Ungarish, and E. Meiburg, Sustained gravity currents in a channel, J. Fluid Mech. **798**, 853 (2016).
[48] D. Bond and H. Johari, Effects of initial geometry on the development of thermals, Exp. Fluids **39**, 591 (2005).
[49] A. C. Lai, B. Zhao, A. W.-K. Law, and E. E. Adams, A numerical and analytical study of the effect of aspect ratio on the behavior of a round thermal, Environ. Fluid Mech. **15**, 85 (2015).
[50] P. Huq, The role of aspect ratio on entrainment rates of instantaneous, axisymmetric finite volume releases of dense fluid, J. Hazard. Mater. **49**, 89 (1996).